catalysts

MDPI

Review

The Applications of Morphology Controlled ZnO in Catalysis

Yuhai Sun [1], Limin Chen [1,2,*], Yunfeng Bao [1], Yujun Zhang [1], Jing Wang [1], Mingli Fu [1], Junliang Wu [1] and Daiqi Ye [1,2]

[1] Guangdong Provincial Key Laboratory of Atmospheric Environment and Pollution Control, School of Environment and Energy, South China University of Technology, Guangzhou Higher Education Mega Centre, Guangzhou 510006, China; sunyuhai1110@163.com (Y.S.); byfcon@foxmail.com (Y.B.); zhangyujun34@163.com (Y.Z.); jing02123204@163.com (J.W.); mlfu@scut.edu.cn (M.F.); ppjl@scut.edu.cn (J.W.); cedqye@scut.edu.cn (D.Y.)

[2] Guangdong Provincial Engineering and Technology Research Center for Environmental Risk Prevention and Emergency Disposal, South China University of Technology, Guangzhou Higher Education Mega Centre, Guangzhou 510006, China

* Correspondence: liminchen@scut.edu.cn; Tel.: +86-20-3938-0508

Academic Editors: Keith Hohn and Leonarda F. Liotta
Received: 29 July 2016; Accepted: 9 November 2016; Published: 30 November 2016

Abstract: Zinc oxide (ZnO), with the unique chemical and physical properties of high chemical stability, broad radiation absorption range, high electrochemical coupling coefficient, and high photo-stability, is an attractive multifunctional material which has promoted great interest in many fields. What is more, its properties can be tuned by controllable synthesized morphologies. Therefore, after the success of the abundant morphology controllable synthesis, both the morphology-dependent ZnO properties and their related applications have been extensively investigated. This review concentrates on the properties of morphology-dependent ZnO and their applications in catalysis, mainly involved reactions on green energy and environmental issues, such as CO_2 hydrogenation to fuels, methanol steam reforming to generate H_2, bio-diesel production, pollutant photo-degradation, etc. The impressive catalytic properties of ZnO are associated with morphology tuned specific microstructures, defects or abilities of electron transportation, etc. The main morphology-dependent promotion mechanisms are discussed and summarized.

Keywords: ZnO; morphologies; polar facets; oxygen vacancies; defects; strong metal-support interactions (SMSI); acid-base properties; electron-hole recombination; band gap; catalytic activities

1. Introduction

ZnO, because of its high electrochemical coupling coefficient, broad radiation absorption range, high chemical stability, and high photo-stability etc., is considered as an attractive multifunctional material [1–4]. Furthermore, ZnO shows attractive applications in optoelectronics, electronics, and laser technology because of its high bond energy (60 meV), broad band gap (3.37 eV), and high mechanical and thermal stability at room temperature [3,4]. Besides, the pyro- and piezo-electric properties of ZnO enable its utilization in sensors, converters and energy generators [5,6]. In addition, extensive research indicates that the properties of ZnO such as photoluminescence (PL), photovoltaics (the conversion of sunlight to electrical power), electron trapping, effective charge separation (charge transfer), the formation of defects, Lewis acid/base properties and strong metal-ZnO interactions, etc., establish its important roles in catalysis including photo-catalysis, photo-electronic catalysis, and thermo-catalysis [7–10]. Most importantly, all of these properties are related to its specific morphologies and nanostructures [7–10].

In most catalytic processes, ZnO is used as a carrier, and therefore, the catalytic properties related to the ZnO structure, especially surface structure, promoted great interest [8,10–15]. Campbell et al. studied the model catalysts, Cu-ZnO single-crystalline and highlighted that Cu-ZnO interactions control their interface structure and stability which is crucial to catalytic performance [16]. Additionally, the previous research indicated that the interface structure is highly morphology-dependent which contributes a lot to the extensive catalytic properties such as promoting the formation of active sites [17,18]. Besides, the optical properties including photoluminescent, cavity resonance feedback (lasing), ultrafast carrier dynamics, spontaneous emission, photo-detection, and wave guiding, have been reviewed in great detail, and are also related to ZnO nanostructures [19,20]. Furthermore, morphology-dependent ZnO electronic properties were also demonstrated by Y. Heo et al. [21]. Thus, it is of great interest to review the morphology-dependent ZnO properties and their roles in catalytic performance.

One- [22–25], two- [26–30], and three-dimensional [29,31,32] ZnO structures under explicit growth conditions have been successfully synthesized. Among them, one-dimensional structures are the main and largest group, including nano-rods [33–35], -tubes [36–38], -belts [39], -wires [40–42], -needles [43], etc. [41,42,44–47]. Besides, two-dimensional structures like nanopellets, nanosheet/nanoplate can also be obtained [48,49]. Examples of three-dimensional morphologies of ZnO include snowflakes, coniferous urchin, flower, dandelion, etc. [50–53]. Except for the explicit growth method, other preparation methods, such as the sol-gel process, vapor deposition, the hydrothermal synthesis, precipitation in aqueous solution, precipitation from microemulsions and mechano-chemical processes, also enable the synthesis of ZnO with different shape, size, and spatial structures. Furthermore, the progress of the synthesis, physical properties, surface chemistry, and applications in devices such as light-emitting devices, photodetectors, optical devices, solar cells, etc. have been extensively summarized [54–73]. Due to the unique properties of ZnO, it has not only been widely investigated in devices; it has also been extensively explored in wastewater treatment by photo-catalysis or water splitting [74–79]. However, the reviewed sewaste water treatments by photo-catalysis performed on ZnO are without special morphologies [74–76] or composite catalysts [77,78] and nanowires [79]. Recently, it was proved that element doping can modify the optical, electrical and magnetic properties of ZnO, so element doped ZnO has been reviewed by several groups [80,81]. Djerdj et al. summarized Co-doped ZnO particularly due to its popular applications in devices [80]. Besides, Samadi et al. made a comprehensive review on various element doping in ZnO, such as transition metal, rare-earth metal, and nonmetal etc., and also discussed their applications in photo-catalysis [81]. Nevertheless, the morphology effects have not been systematically investigated in the doped photo-catalysts. Therefore, although there are abundant reviews related to ZnO, there is still lack of a systematic summary on the applications of morphology controlled ZnO in catalysis.

Concerning the most important technique of water photolysis, it is a sustainable technology to convert natural solar energy and water into chemical fuels and is thus considered a complete solution to the forthcoming energy crises. Furthermore, solar-powered water splitting using photo-electrochemical (PEC) cells is considered to be essential for the success of a hydrogen energy system [82–84]. In addition, in most water splitting research, photo-electrochemical (PEC) cells are focused on one-dimensional ZnO-based materials. Therefore, water splitting by ZnO photocatalysis is mainly concentrated on the development of ZnO band gap engineering, not the morphology [85–94]. Therefore, water splitting by ZnO photocatalysis is not covered here.

Besides, the extensively studied photocatalysis in waste water treatment and water splitting, ZnO is also utilized in very important energy related thermo-catalytic reactions, such as CO_2 hydrogenation to fuels, methanol steam reforming to generate H_2, bio-diesel production, etc. and photo-assisted electro-catalysis such as photoelectrooxidation of alcohol, etc.; however, no reviews coveres these morphology-dependent reactions.

Thus, this review mainly focuses on ZnO morphology-dependent catalytic processes and tries to reveal the relationship between catalytic performance and its morphology related properties. Moreover,

the properties and catalytic applications of element doped ZnO with specific morphologies are also covered and discussed concurrently. The catalytic reactions not only cover the comprehensively explored photo-degradation of organic pollutants but also cover the synthesis of methanol, methanol steam reforming, alcohol oxidation, CO oxidation, hydro-desulfurization (HDS), bio-diesel production, photocatalytical removal of inorganic pollutants like NO_x and Cr(VI) as well as photo-assisted electro-catalytic reactions, etc.

2. Applications to Thermo-Catalysis

2.1. Methanol Synthesis

The synthesis of methanol, higher alcohols, gasoline, and related higher hydrocarbons (Fischer-Tropsch-like reactions) through CO_2 hydrogenation have received much renewed attention, especially methanol because of its indispensable position in the present fuel and chemical infrastructures [95]. Among the different kinds of studied catalystic systems, $Cu/ZnO/Al_2O_3$ based catalysts are the most promising ones [96,97]. According to previous publications, ZnO morphology plays a vital role in the catalytic performance of CO_2 hydrogenation to methanol [10,18]. Schimpf et al. prepared Cu-Zn colloids and applied them to methanol synthesis [18]. Through a morphology controllable synthesis, spherical Cu attached to the truncated edges of triangular ZnO prisms was obtained and its methanol productivity (6408 $\mu mol_{CH3OH} g_{Cu}{}^{-1} \cdot h^{-1}$) was much higher than that of Cu-Al (2280 $\mu mol_{CH3OH} g_{Cu}{}^{-1} \cdot h^{-1}$) and traditional $Cu/ZnO/Al_2O_3$ (6222 $\mu mol_{CH3OH} g_{Cu}{}^{-1} \cdot h^{-1}$) catalysts. What is more, the catalyst active structure was determined as spherical Cu attached to the truncated edges of triangular ZnO prisms, which were proposed to serve as reservoir for ZnO_x species and promote the catalytic activity. As already known, catalytic processes usually occur on the surface of the catalysts, and the impressive catalytic properties are usually due to the small catalyst size which leads to a high metal surface area, the high metal-support contacting efficiency, as well as the catalyst chemical composition. Except for the factors mentioned above, the strong metal-support interactions (SMSI) were also considered as a significant factor to influence catalytic performance [12,15,98,99]. Liao et al. reported significant morphology-dependent Cu-ZnO interactions and revealed their promotional effects on the catalytic performance of CO_2 hydrogenation to methanol [10]. In their work, ZnO nanorods and nanoplates were synthesized and physically mixed with Cu nanoparticles and Al_2O_3 in order to test the catalytic properties of CO_2 hydrogenation. The evident shape effects of ZnO on its interaction with copper were identified. The research demonstrated that the catalyst, Cu/ZnO nanoplate$/Al_2O_3$ with exposed polar ZnO (002) facet, exhibited much higher methanol selectivity (70%) compared with that of Cu/ZnO nanorod$/Al_2O_3$ (40%) catalyst. The advanced catalytic property was attributed to the strong interactions between (002) facet of ZnO plate and Cu, because the electrons of the ZnO nanoplate at the conductive band could transfer to the Cu Fermi level, increasing the concentration of oxygen vacancies. Furthermore, the higher electron trapping properties of ZnO nanoplate promote defects formation. In addition, different surface electronic structures were also thought to enhance SMSI [100]. All of these properties are related to the existence of polar ZnO nanoplate; therefore, the supported catalysts displayed superior CO_2 hydrogenation activity to methanol. Very recently, ZnO hexagonal nanoplate loaded Cu nanoparticles were successfully modified by a heating approach and their catalytic performance was evaluated [101]. The as-prepared catalysts are highly selective for methanol production in comparison with Cu/rod-like ZnO which is due to the much stronger interactions between Cu and the exposed polar (002) facet in plate-like ZnO and a greater number of oxygen vacancies caused by the polar facets. Furthermore, CO_2 was probably activated by the generated vacancies and the surface Cu species could facilitate molecular rearrangement (formate) and hydrogenation to produce methanol. Similarly, Lei et al. prepared different morphology ZnO structures (rod-like and filament-like) with Cu support and compared their catalytic activities for CO_2 hydrogenation [102]. The Cu/ZnO (filament-like) catalyst displayed better catalytic activity which was due to stronger Cu-ZnO interaction and more oxygen vacancies

caused by the higher exposure of the (002) polar face. Except for the morphologies mentioned above, a Cu-decorated ZnO nanotube model system was produced by Güder et al. to investigate the effects of ZnO morphology on the CO_2 hydrogenation performance [103]. Although the engineered catalyst exhibited 70 times higher CO_2 activation capability because of its high ZnO surface area compared with the commercial one, it showed a lower CH_3OH yield. This is mainly because of the high surface mobility of Cu, where intermediate species, such as HCOO, HCOOH, H_2COOH, HCO, H_2CO, and H_3CO, do not remain stable enough with moving particles to form CH_3OH. Thus, a better catalytic performance is not only determined by the high support surface area, but also by the low surface mobility of Cu.

2.2. Methanol Steam Reforming (MSR)

Methanol steam reforming (MSR) has been extensively studied for hydrogen production [104–107], primarily because of low sulfur content, low carbon/hydrogen ratio, and the relatively low reforming temperature (200–300 °C) of methanol. In order to achieve a compact and highly efficient fuel cell system, a MSR catalyst with high activity and selectivity is essential [108]. ZnO has also been considered as an effective catalyst component for methanol reforming to hydrogen [109–113]. Being similar to the methanol synthesis, the catalytic system of MSR is also commonly made up with Cu-Zn-Al. Lin et al. designed a core-shell nano-structured catalyst, a ZnO nanorod (NR) core with Cu nanoparticles shell (NPs, NR@NPs), and tested their properties for the MSR reaction [113]. The as-synthesized Cu-ZnO catalyst achieved a high methanol conversion rate of about 93% which is apparently higher than the commercial one. The superior catalytic property and stability of ZnONR@CuNPs was mainly due to the large surface area of the core-shell nanostructure which enhanced the Cu dispersion and facilitated the surface contact efficiency between the catalysts and reactants. Apart from the traditionally used Cu-ZnO system, Karim et al. considered the effects of ZnO morphology on the PdZn catalytic system [114]. In their research, Pd supported on ZnO nanorod catalyst showed the highest catalytic activity compared to anomalous and surface etched ZnO. The authors stated that the catalytic activity was greatly influenced by the ZnO morphologies instead of the Pd particle size or Pd-Zn alloy particle size/composition. The larger the amount of faceted ZnO, the higher is the catalytic activity. Furthermore, the morphology controlled ZnO not only served as the support and Zn source for the Pd-Zn alloy formation, but also facilitated one of the intermediate formation steps in MSR. Then, Zhang et al. intensively investigated the effects of ZnO surface polarity (needle-like ZnO crystallites predominantly exposed non-polar facets and commercial ZnO without any dominant facets) on the catalytic properties of MSR [13]. Different from the research mentioned above, they stressed the significant roles of Pd-Zn alloy. CO selectivity was determined by the Pd_xZn_y alloy structure and particle size which could be influenced by ZnO non-polar facet. Pd-rich phases (Pd_xZn_y, $x > y$) were formed predominantly at low Pd loadings on both ZnO-N (mainly non-polar facets) and ZnO-P (no predominant polar facets) supports, resulting in high CO selectivity. With similar Pd loading, Pd/ZnO-P gave lower CO selectivity than Pd/ZnO-N. This was due to more facile stability of Pd-Zn_β ($x/y = 1$) on polar ZnO (0001) instead of non-polar facets, which led to a higher CO_2 selectivity. In addition, the particle size of Pd_xZn_y alloy has been reported to be correlated to the CO selectivity in MSR. Much smaller Pd_xZn_y alloy size was observed on ZnO-N, which also showed higher CO selectivity. Also, this result was in accordance with previous studies [114–116]. Obviously, ZnO morphology has a great impact on the Pd-Zn alloy structure and product selectivity. Interestingly, Halevi et al. [117] also reported the effects of polar (plate-like) ZnO on the formation of Pd-Zn alloy and product selectivity for MSR. In their research, 50% higher specific activity and ~70% CO_2 selectivity was obtained over plate-like ZnO supported Pd catalyst compared with the commercial one, with a lower amount of ZnO polar surfaces (Figure 1). The The density functional theory (DFT) calculation study indicated that the lowest activation energy and highest specific activity over plate-like ZnO based catalyst was ascribed to the higher proportion of ZnO polar facets. Then, the thermal reduction was found to reduce CO_2 selectivity over plate-like ZnO, which also caused defect formation and surface

reconstruction. This suggested that the MSR active sites on ZnO are defects formed on the polar facets of ZnO. Eblagon et al. studied the influence of the different morphologies of ZnO (prevalent nanorods from Sigma-Aldrich, spherical nanoballs were assembled by nanosheets obtained by calcination of ZnO in O_2, air, N_2, and H_2) on the catalytic performance of ZnO supported Pd catalysts in the MSR reaction [118]. The most active and ultraselective catalyst was Pd/ZnO-calcined in H_2. The superior catalytic performance was attributed to the high amount of oxygen vacancies which acted as additional active sites for water adsorption and subsequent activation, and also drastically suppressed the formation of CO by replenishment of oxygen vacancies, thus leading to high H_2 selectivity in the MSR reaction.

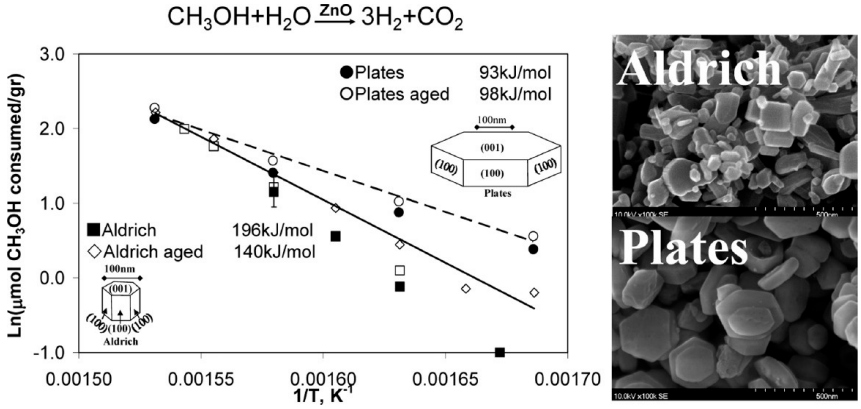

Figure 1. Arrhenius plot for ZnO samples: (●) plates; (○) plates aged; (■) Aldrich; (□) Aldrich repeated; (◇) Aldrich aged. Reproduced with permission from [117]. Copyright American Chemical Society, 2013.

Besides the MSR reaction, the impressive morphology-dependent promotion effects of ZnO were also found on combined reforming hydrogenolysis (CRH) of glycerol by Hu et al. [11]. Hexagonal ZnO disk- and rod-crystals with different length to diameter aspect ratios were controllably prepared and employed as co-catalysts with rapidly quenched skeletal NiMo catalyst in the CRH of glycerol. The data demonstrated that non-polar facets contributed to the prominent selectivity of the hydrogenolysis products and high production rate of 1,2-propandiol (1,2-PDO). Furthermore, there was an excellent linear relationship between the TOF of 1,2-PDO and the surface area of ZnO (100) non-polar facets. Further investigation indicated that CO_2 was chemisorbed on ZnO (100) non-polar facets to form a stable tridentate carbonate species. The C atom of CO_2 bonded to O anion in non-polar (100) facets, both O atoms of CO_2 formed the equivalent bonds with Zn cations nearby. This CO_2 chemisorption mode altered the occupied and unoccupied surface of Zn sites, leading to a more electron-deficient unoccupied Zn cation, enhancing the Lewis acidity of non-polar facets. In contrast, ZnO (001) polar facets terminated solely with Zn^{2+} or O^{2-} ions, so such a type of CO_2 adsorption mode cannot be adopted. Therefore, on the non-polar facets, this type of CO_2 adsorption-enhanced Lewis acidity greatly accelerated the dehydration of glycerol to acetol and the intermediate transformation to 1,2-PDO, which was considered to contribute to the significant morphology-dependent promotion effects of ZnO.

2.3. Biomass Related Catalytic Reactions

With the decrease of petroleum reserves and the increase of environment protection consciousness, bio-diesel, as a renewable energy source, has been considered to be a significant alternative to petroleum based diesel fuel over recent years [119,120]. Bio-diesel produced through hydrolysis-esterification reactions has attracted great interest [121–123]. Liu et al. prepared perfect hexagonal sectional ZnO "multi-level tower" (Figure 2) based catalysts to produce bio-diesel [124]. In comparison with ZnO particles, the multi-level tower ZnO achieved 73.5% bio-diesel yield, about 60% higher than that of

ZnO particles. They believed that multi-level tower ZnO predominantly exposed active O^{2-} on $(10\bar{1}0)$, $(\bar{1}100)$, $(01\bar{1}0)$, and (0002) facets. As reported, O^{2-}, in the layer structured Mg-Al hydrotalcites and MgO, is considered as the predominantly strong basic sites to catalyze bio-diesel production [125]. Besides, methanol molecules prefer sticking to ZnO facets with higher concentration of O atoms, such as (102) and (103) facets. On the contrary, ZnO (112) facets contains higher concentration of Zn and the adsorption of carbonyl groups are preferred [126,127]. Thus, these surfaces were considered as the active centers of trans-esterification and esterification reactions [128]. According to this research, it is the ZnO predominantly exposed active basic O^{2-} on $(10\bar{1}0)$, $(\bar{1}100)$, $(01\bar{1}0)$ and (0002) facets that contribute to the apparent increase of the catalytic activity and bio-diesel yield. Except for bio-diesel production, the transformation of biomass derived products to value added chemicals is also very attractive in the biomass chemical industry, for example, the conversion of bio-ethanol to acetaldehyde or acetone. Zhang et al. investigated the influence of needle-like and flake-like ZnO (ZnO-N and ZnO-F, respectively) on the catalytic performance of bio-ethanol conversion to acetone [129]. There is a large amount of water in bio-ethanol and they found distinct water activation on polar/non-polar facets of ZnO nanoparticles. Water was strongly adsorbed on ZnO $(001)/(00\bar{1})$ polar facets, which prohibits the formation of the oxygen vacancy and thus the adsorption/dissociation of H_2O on the ZnO-F. Thus, the conversion rate of ethanol to acetaldehyde on ZnO-F is much higher than that on ZnO-N. However, the subsequent acetaldehyde conversion to acetone via the ketonization pathway mainly occurs on the ZnO (100) non-polar facet on which water dissociation is highly favored. Therefore, acetone selectivity on ZnO-N with dominant (100) non-polar facets is always higher than that on ZnO-F with $(001)/(00\bar{1})$ polar facets. In comparason, ethanol conversion to acetaldehyde was also explored and a structure-surface-sensitivity phenomenon was observed [130]. The results indicated the presence of particular acidic hydroxyl groups on the polar surfaces are responsible for the high selectivities to minor products, ethylene, and condensation products. Therefore, it is necessary to minimize the polar surface extension as well as control the acid-base properties in ZnO materials to optimize the dehydrogenation performance towards acetaldehyde as the main product.

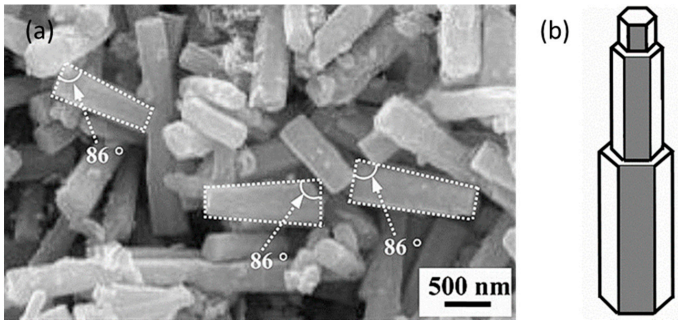

Figure 2. Scaning electron microscopy (SEM) morphology (**a**) and configuration profile (**b**) of "multi-level tower". Reproduced with permission from [124]. Copyright Elsevier, 2011.

2.4. CO Oxidation

The CO oxidation reaction is a simple but important reaction and it is usually utilized as a probe reaction to investigate various catalytic theories. Shape-dependent promotion effects have been extensively explored especially over rod-shaped oxides [131–136]. Liu et al. [137] synthesized Au/ZnO-NW (ZnO nanowires) and Au/ZnO-P (powders) and evaluated their catalytic properties for CO oxidation. Au/ZnO-P provided higher CO oxidation activity with a rate of 2.09 $mol_{CO}g_{Au}{}^{-1}\cdot h^{-1}$ at 100 °C but dramatically decreased to 0.52 and 0.062 $mol_{CO}g_{Au}{}^{-1}\cdot h^{-1}$ (an activity drop of around 4- and 34-times) when calcined at 400 °C and 600 °C, respectively. However, only 1.6- and 7-times decreases were observed over Au/ZnO-NW catalyst, when calcined at 400 °C and 600 °C, respectively. Generally, the low energy $(10\bar{1}0)$ facet predominated ZnO-NW is more stable than ZnO-P, which consists of various highly active high-energy surfaces. So, when calcined at high temperature, although there are much

stronger interactions between Au nanoparticles and ZnO-P, Au on ZnO-P are less resistant to sintering than those on ZnO-NW due to the high activity of ZnO-P. Therefore, Au/ZnO-NW with relatively weaker interactions between Au and ZnO-NW displayed higher stability at high pretreatment temperature. In addition, Liu et al. further explored the catalyst stability [138]. After calcination at 600 °C, the CO oxidation rate decreased about 30-times on Au/ZnO (powder) but only about 4-times on Au/ZnO (nanowires). They claimed that the well-defined surface structure of the ZnO NWs and their strong interfacial interactions with Au NPs are beneficial for the formation of a heteroepitaxy structure. Besides, the impressive stability was ascribed to the unique interactions between Au NPs and the $(10\bar{1}0)$ nano facets of the ZnO NWs.

Liu et al. studied the CO oxidation reaction over ZnO nanorods supported Au catalysts and proposed the existence of O-SMSI and R-SMSI between ZnO nanorods and Au nanoparticles [139]. The O-SMSI in Au/ZnO occurred under oxidative pretreatment conditions while the R-SMSI took place in reductive pretreatment conditions, the same as the classical SMSI (Figure 3). Both SMSI effects in the Au/ZnO system however do invoke mass transportation and charge re-distribution. In the O-SMSI, under oxidative pretreatment conditions, the formation of Au-O-Zn linkages are vital in driving ZnO to the Au surface; while the formation of Au-Zn alloy was thought to be of great importance in the R-SMSI. Also, the existence of O-SMSI or R-SMSI might be led by the n-type semiconductor properties or non-polar surface of ZnO. It is interesting that Au/ZnO with R-SMSI showed a lower CO oxidation activity compared with that of with O-SMSI. Therefore, it was claimed that the catalytic activity greatly depends on the formation of Au-O-Zn linkage or Au-Zn alloy under different pretreatment conditions.

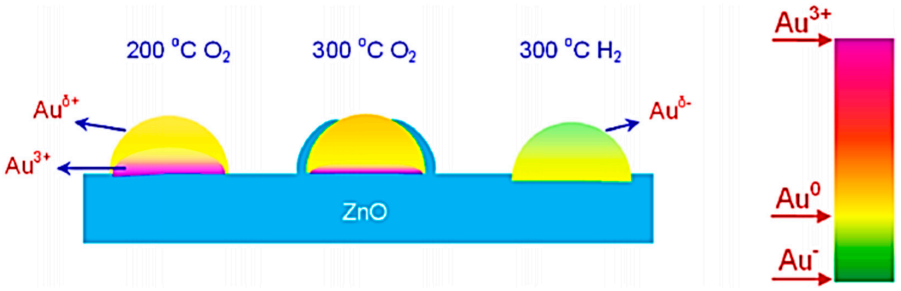

Figure 3. Schematic illustration for the strong metal-support interactions (SMSI) states in the Au/ZnO nanorod system under various pretreatments. The color bar depictsthe sign and degree of charging of the gold nanoparticles. Reproduced with permission from [139]. Copyright American Chemical Society, 2012.

Besides, three different morphologies of ZnO, prepared by chemical vapour deposition (ZnO_{CVD}), two commercial samples from Strem Chemicals (ZnO_{SC}) and Evonik (ZnO_{EV}), were used to support 1 wt % Au to explore the SMSI in CO oxidation [140]. At room temperature, the best results were obtained over ZnO_{CVD} which showed a CO oxidation activity of 2 $mol_{CO}g_{Au}{}^{-1}\cdot h^{-1}$. Its high-resolution electron microscopy images indicated a lot of Au nanocrystals epitaxially oriented on ZnO rods which means the SMSI lead to such a unique structure, and the unique metal-support interactions were proposed to be associated with the enhanced catalytic activity. Recently, Liu et al. [141] designed a new method to produce highly dispersed Au clusters on ZnO meso-crystal through a ZnO defect-mediation method. Au clusters were supported on and/or doped in defect-rich twin-brush ZnO (TB-ZnO) meso-crystals (Figure 4), marked as Au/ZnO:Au. This sample exhibited remarkably high activity in CO oxidation about 8.21 $mol_{CO}/g_{Au}\cdot h$ (or 9.35×10^{-5} $mol_{CO}/g_{cat}\cdot s$). This is much higher than that of the Au/TiO_2 or $Au/FeTiO_2$ system [139]. The large amount of Zn- and O- vacancy defects in TB-ZnO provide a strong driving force for the introduction of Au into the lattice of ZnO (Figure 5). The ZnO meso-crystal thus behaved like a sponge to accommodate the large number of Au atoms. These Au atoms eventually moved out of the ZnO lattice to form highly dispersed Au nanoparticles of around 2 nm, after moderate thermal treatment. The DFT calculation showed the Au-doping in

TB-ZnO and the facile defect-mediated migration of Au in it, are both energetically favorable. This was also thought to be the novel explanation of the SMSI between the Au and ZnO support which therefore could greatly enhance the catalytic activity. In summary, the morphology-dependent SMSI between Au nanoparticles and ZnO was thought to be the main reason for the high activity and stability in CO oxidation. Interestingly, Mg^{2+} doped hierarchical flower-like ZnO microspheres assembled by porous nanosheets were developed to load Pd catalyst for CO oxidative coupling activity to dimethyl oxalate (DMO) [142]. Additionally, the effects of Mg^{2+} doping on the catalyst stability were investigated. The doped ZnO supported catalyst can not only retain the catalytic activity of undoped ZnO supported catalyst, but also display obviously higher stability. This is mainly due to the formation of Zn-Mg oxide solid solution in doped ZnO, which leads to a strong metal-support interaction, caused by the electron transfer from the ZnO substrate to Pd NPs, and this SMSI was proved to effectively restrain the sintering of the active Pd NPs, suppressing the growth of Pd NPs, and thus, enhancing the catalytic stability.

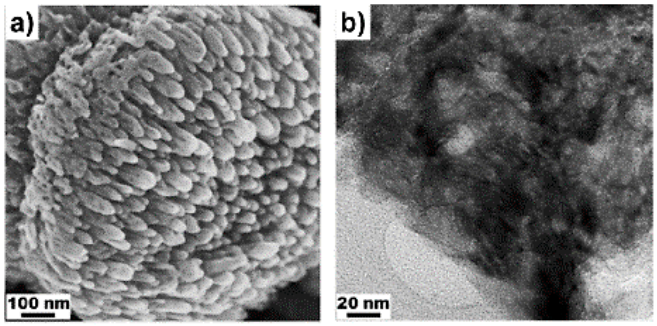

Figure 4. (**a**) SEM image of calcined TB-ZnO mesocrsytal; (**b**) transmission electron microscopy (TEM) image of the sliced as-prepared Au/TB-ZnO. Reproduced with permission from [141]. Copyright American Chemical Society, 2015.

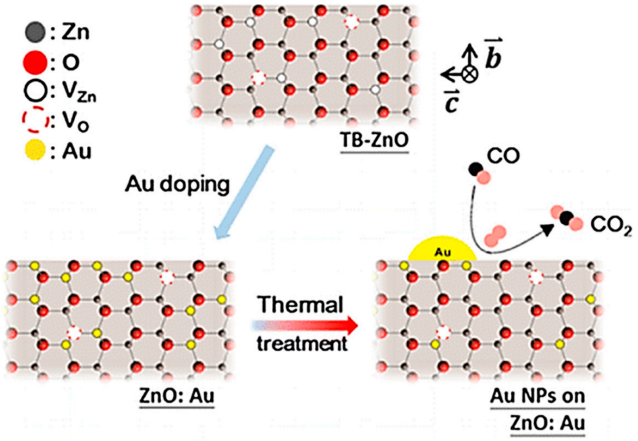

Figure 5. Schematic illustration for Au-doped defect-rich TB-ZnO and their catalytic process. Reproduced with permission from [141]. Copyright American Chemical Society, 2015.

2.5. Other Thermo-Catalytic Reactions

Generally, hydro-desulfurization (HDS) catalysts are alumina- or silica-supported molybdenum, cobalt and nickel catalysts but achieving completely sulfur free fuels by catalytic HDS processes is still a great challenge [143–147]. Petzold et al. claimed that ZnO nanowire supported nickel catalysts were the most advanced HDS catalysts which could produce ultra-low sulfur diesel oil [148]. They confirmed that proper ZnO supports can ensure the generation of a highly active nickel species during deep desulfurization via the reported regenerative method. The in-situ heating investigation revealed that

when Ni precursor was impregnated on ZnO nanowire it displayed a high dispersion, due to strong metal-support interactions, resulting in smaller NiO and Ni particle sizes, compared with Ni loaded on spherical ZnO nanoparticles (NPs). Besides, the highly active Ni-Zn alloy for HDS of thiopenes was preferentially formed during the reduction step. According to the previous publication, the SMSI could promote sulfur transfer from NiS to ZnO [147]. Therefore, the short diffusion paths between Ni and ZnO and the strengthened metal-support interactions led to the enhancement of sulfur uptake capacity and catalytic activity.

Exept for the above mentioned energy related thermo-catalytic reactions, morphology-controlled ZnO was also applied in environment pollutant removal processes. For example, Tang et al. studied the effects of exposed (0001) facets over ZnO micro/nanocrystals on the catalytic performance of thermal decomposition of ammonium perchlorate (AP) [149]. It was found that a higher percentage of exposed (0001) facets leads to lower activation energy of AP decomposition. Furthermore, the DFT calculation reveals that the highly exposed (0001) facets will promote perchloric acid adsorption and diffusion and facilitate the formation of active oxygen species, leading to the more complete oxidation reaction of ammonia in the catalytic decomposition of AP.

For thermo-catalysis, the morphology effects of ZnO are summarized in Table 1; the corresponding promotion mechanisms are illustrated in Figure 6 and as follows:

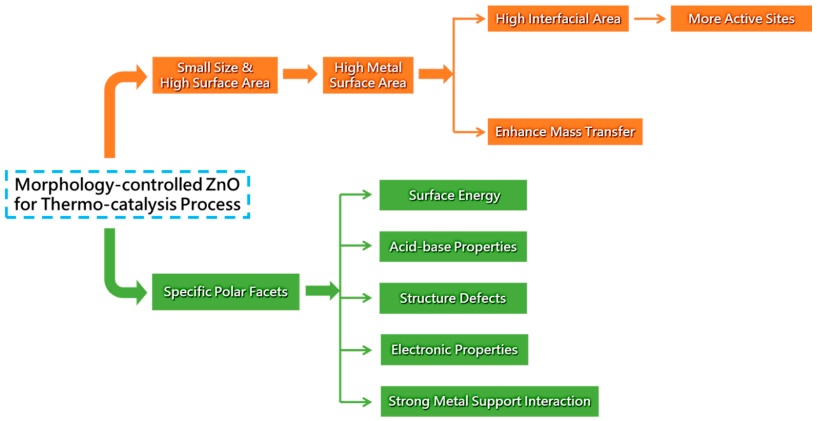

Figure 6. Promotion mechanism illustration of morphology controlled ZnO in the thermo-catalysis process.

(1) Small size. Small particle size means high metal surface area which enables high metal-support contact area (interfacial area), enhancing interface interactions, and tuning catalytic performance. On the other hand, small particle size means more accessible active sites.

(2) Tuning the metal-support interactions even changing the types of SMSI. The SMSI are different between various morphologies of ZnO supported metal. Besides, the alloy and defects (oxygen vacancies), etc. produced by synergy or SMSI effects between the active metal and support also contribute to the high catalytic activities.

(3) Guaranteeing a certain catalytic stability. The exposed ZnO facets are proved to have different facet energy which could influence the interactions between metal and support. Both SMSI and the stability of different morphologies of ZnO play important roles in the sintering properties of the supported metal nanoparticles during the catalytic and pretreatment processes.

(4) Electronic properties and defects. Generally, different morphologies will expose different facets which will cause great diversity of electronic properties, defect types, and concentrations. All of these contribute to the capacity of electron trapping or changing the electron structures.

(5) Catalyst surface acid-base properties. The polar and non-polar facets show different surface acidity-basicity and O^{2-} is proved to be the predominantly strong basic site. Besides, the different concentrations of oxygen and zinc atoms on various facets tend to adsorb different reactant molecules which can be used to adjust target product selectivity.

Table 1. The applications of morphology controlled ZnO in the thermo-catalytic process.

Type of Catalytic Reactions	Catalyst	ZnO Morphology	Morphology-Dependent Promotion Mechanisms	Reference
Methanol synthesis	Cu-ZnO	Triangular	The formation of Cu-Zn colloids act as reservoir for ZnO_x species	[31]
	$Cu/ZnO/Al_2O_3$	Nanoplates, Nanotubes	The exposure of ZnO (002) polar facets which enhances the SMSI, promotes electron transportation and leads to the formation of oxygen vacancies	[10]
	Cu-ZnO	Nanoplates	The exposed polar (002) facets in plate-like ZnO showed a much stronger interaction with Cu and a higher number of surface oxygen vacancies existed at the materials' interface. Thus CO_2 was likely to be activated by the generated vacancies and the Cu phase at the interface assisted molecule rearrangement (formate) and hydrogenation to methanol	[101]
	Cu-ZnO	Nanorods filament-like	The stronger Cu-ZnO interaction and more oxygen vacancies caused by the more exposure of (002) polar face	[102]
	Cu-ZnO	Nanotubes	High surface area leads to an excellent CO_2 conversion; the high surface mobility of Cu results in low methanol selectivity	[103]
Methanol steam reforming	Cu-ZnO	Nanorods	The large surface area enhances Cu dispersion, offers an effective surface contact between reactants and catalysts and enhances SMSI	[113]
	Pd-ZnO	Nanorods	The morphology controlled ZnO not only acts as the support and Zn source for Pd-Zn alloy, but also facilitates one of the intermediate formation steps in MSR	[114]
	Pd-ZnO	Needle-like	Exposure of ZnO non-polar facet will influence Pd-Zn structure and particle size to influence product selectivity	[13]
	Pd-ZnO	Nanoplate	Plate-like ZnO possesses the lowest activation energy that leads to the highest specific activity	[117]
	Pd-ZnO	Nanoballs assembled by nanosheets	Higher oxygen vacancy concentration results in the high H_2 selectivity in MSR reaction	[118]
Combined reforming hydrogenolysis of glycerol	NiMo-ZnO	Nanodisk, Nanorods	CO_2 adsorbed on the (100) non-polar plane can make the un-occupied Zn cations more electron-deficient, enhancing the Lewis acidity of the non-polar plane	[11]
Bio-diesel production	ZnO	Multi-level tower	Multi-level tower ZnO predominantly exposed active O^{2-} on (0002), $(10\bar{1}0)$, $(\bar{1}100)$ and $(01\bar{1}0)$ facets shows strong basic sites that results in obvious enhancement of catalytic activity and high yield of bio-diesel	[124]
Bio-ethanol conversion	ZnO	Needle-like, Flake-like	H_2O was strongly adsorbed on ZnO $(001)/(00\bar{1})$ polar facets which prohibits the formation of the oxygen vacancy and thus adsorption/dissociation of H_2O, leading to high ethanol conversion rate but low acetone selectivity. Acetaldehyde reaction to form acetone via the ketonization pathway mainly occurs on the ZnO (100) non-polar facet on which water dissociation is highly favored	[129]
Ethanol conversion	ZnO	Brick, Disk, Needle prism	The presence of acidic hydroxyl groups on polar surface seems to be responsible for the formation of ethylene and condensation products.	[130]

Table 1. *Cont.*

Type of Catalytic Reactions	Catalyst	ZnO Morphology	Morphology-Dependent Promotion Mechanisms	Reference
CO oxidation	Au-ZnO	Nanowires	Compared with Au/ZnO-P exposing various highly active ZnO facets, although Au/ZnO-NW catalyst predominantly exposing stable low energy ZnO ($10\bar{1}0$) facets, exhibited relatively weaker interactions between Au nanoparticles and ZnO. It is mainly because of the higher stability of ZnO-NW that prohibits the sintering of Au particles and then displays higher stability at high pretreatment temperature	[137,138]
	Au-ZnO	Nanorods	The formation of Au-O-Zn linkage or Au-Zn alloy was caused by different SMSI due to different pretreatment conditions.	[139]
	Au-ZnO	Nanorods	The SMSI leading to a unique structure of a number of gold nanocrystals epitaxial oriented on the ZnO nanorod	[140]
	Au-ZnO	Twin-brush	The SMSI lead to a large amount of Zn- and O-vacancy defects in TB-ZnO which provides a strong driving force for introducing gold particles into the lattice of ZnO which then eventually move out of ZnO lattice to form highly dispersed Au nanoparticles	[141]
	Mg-ZnO (doping)	Flower-like ZnO microspheres	Mg^{2+} doped ZnO support promotes a strong metal-support interaction caused by the formation of Zn-Mg oxide solid solution, effectively restrain the sintering of the active Pd NPs; retard the growth of Pd NPs, and enhance the catalytic stability	[142]
Hydro-desulfurization	Ni-ZnO	Nanowires	ZnO supports can ensure the generation of highly active nickel species during deep desulfurization through the reported regenerative step. The enhanced metal-support interactions and short diffusion paths between Ni and ZnO NWs lead to improved activity and sulfur uptake capacity	[148]
Decomposition of ammonium perchlorate	ZnO	Nanorods Nanoplates	Highly exposed (0001) facets will promote perchloric acid adsorption and diffusion and facilitate the formation of active oxygen species, leading to the more complete oxidation reaction of ammonia in the catalytic decomposition of AP	[149]

In summary, ZnO with various morphologies will expose different facets, polar or non-polar, which present different electronic properties and surface energy. So, this on the one hand will result in different SMSI, leading to different catalyst chemical states, catalyst particle size, metal-support contact area, and catalyst stability. All of these influence their catalytic properties. On the other hand, polar or non-polar facets possess diverse types and concentrations of oxygen vacancies and different acid-base properties, which also tune their catalytic properties.

3. Applications to Photo-Catalysis

Apart from thermo-catalytic reactions, morphology controlled ZnO has also been widely used for environmental pollutant mineralization, degradation and water splitting to hydrogen due to its large band gap and low cost of fabrication [150]. Furthermore, in some cases, ZnO displays dramatically impressive photo-catalytic activities compared with broadly studied TiO_2 [88,91,151–160]. In addition, element doping including both metal and nonmetal (C, N, S) doping could lead to an enhanced photo-catalytic activity; interestingly, most non-metal dopings were reported in photo-catalytic water splitting [161–168].

3.1. Degradation of Organic Dyes

3.1.1. Degradation of Methylene Blue (MB)

MB is a typical organic dye in waste water and its degradation attracts great interest. Jang et al. made a comparison of MB photo-catalytic degradation properties between ZnO nanoparticles and nano-crystalline particles [169]. The results revealed that ZnO nanoparticles were more effective than nano-crystalline particles and the higher photo-catalytic activity over ZnO nanoparticles was ascribed to the higher specific surface area compared with ZnO nano-crystalline particles. In comparison with spherical ZnO quantum dots (QDs), the enhanced photo-catalytic properties of MB decomposition over hexagonal faceted ZnO prism QDs with polar surfaces was reported by Zhang et al. [170]. The better photo-catalytic properties were due to the following three reasons. First, hexagonal ZnO QDs possess smaller sizes which lead to a larger specific surface area. Second, there are more surface defects on hexagonal ZnO QDs which generate more oxygen vacancies. Third, the hexagonal ZnO QDs have more polar O-terminated $(00\bar{1})$ and Zn-terminated (001) facets which are facile to the adsorption of oxygen molecules and OH^- ions, leading to higher generation rate of H_2O_2 and OH· radicals.

Except for the above mentioned QDs, Mclaren et al. prepared regular hexagonal plate-like ZnO nano-crystals and hexagonal rods with various lengths through a simple solution method [171]. The hexagonal plate-like ZnO displayed more than 5-times higher photo-catalytic activity in the MB photo-catalytic degradation compared with rod-shaped ZnO (Figure 7). This may be due to the terminal polar (001) and $(00\bar{1})$ facets on hexagonal plate-like ZnO which are more active for photo-catalysis than the non-polar surfaces on hexagonal rods. Similarly, Duan et al. [172] explored the photo-degradation efficiencies of MB over ZnO plates, hexagonal prisms, and rose-like twinned ZnO crystal films. Interestingly, the photo-degradation efficiencies of MB over hexagonal prisms and rose-like twinned ZnO crystal films were 95% and 96%, respectively. The excellent photo-catalytic properties were due to the high percentage of polar facets and high oxygen vacancy concentrations which decreased in the order of rose-like > hexagonal prisms > ZnO plates. Later, many other groups synthesized different morphologies of ZnO and claimed that the enhanced photo-activities were due to the high exposure of polar facets and large number of oxygen vacancies [173–178].

Jeong et al. also compared the photo-catalytic performance of ZnO nanorods and nanoplates [179]. On the contrary, they discovered that ZnO nanorods were more active for the degradation of phenol and MB, and the generation of OH· radicals and photocurrents. All of these were related to single-electron transfer reactions. ZnO plates (different from hexagonal plate-like nano-crystals mentioned above, which seem more like nano-sheets, Figure 8), were more effective for the two-electron transfer initiated reactions, such as the production of hydrogen peroxide and molecular hydrogen. X-ray

photoelectron spectroscopy (XPS) and photoluminescence (PL) spectra characterization confirmed that ZnO nanorods had more pronounced oxygen vacancies near the conduction band energy level, facilitating electron trapping, and therefore, enhancing the hole transfer reactions in ZnO rods. In comparison, ZnO plates here possessed relatively pronounced oxygen interstitial contributions near the valence band energy level, promoting hole trapping, enhancing the availability of photo-generated electrons, and being favorable for multi-electron transfer reactions. This example demonstrates the effects of morphology-dependent charge transfer on photo-degradation mechanisms.

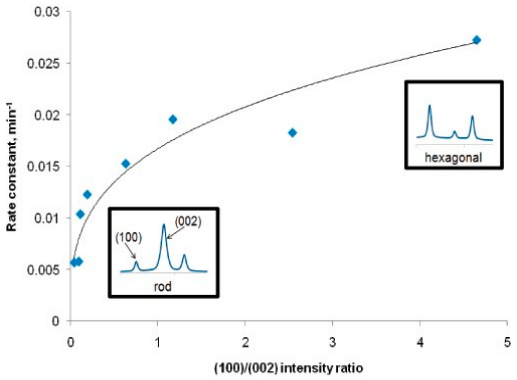

Figure 7. Plot of the rate constants vs. (100)/(002) intensity ratio. Reproduced with permission from [171]. Copyright American Chemical Society, 2009.

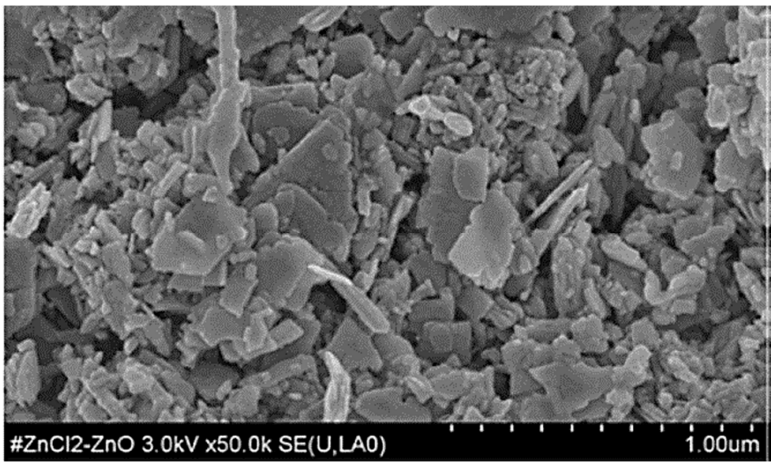

Figure 8. Field emission scanning electron microcopy (FE-SEM) image of ZnO plates. Reproduced with permission from [179]. Copyright American Chemical Society, 2014.

Except for the above mentioned roles of morphology-dependent oxygen vacancies, the other important roles of oxygen vacancies in morphology controlled ZnO were intensively studied by Khokhra et al. [180]. Flower-like interwoven grown ZnO nano-sheets and un-aggregated nanosheets were prepared and tested for photo-degradation of MB. The excellent photo-degradation efficiencies of flower-like interwoven grown sheets (99.94%) after 120 min irradiation are ascribed to the faceted geometry, large surface area of ZnO nanosheets, and high surface oxygen vacancies which narrow the band gap as proved by photoluminescence spectra. Therefore, the oxygen vacancies not only serve as photo-induced charge trap centers or active centers but also narrow the ZnO bandgap by broadening of the valance band. The narrowing of the energy band gap expanded the adsorption band of visible light, increasing photo-catalytic activity under sunlight irradiation. Thus, this advanced property is attributed to the surface oxygen vacancies which could narrow the band gap and generate more effective charges.

In spite of the roles of specific surface area, polar facets and oxygen vacancies, Wang et al. focused on the roles of Zn sites [181]. They prepared the flower-, spindle-, sword- and umbella-like ZnO architecture with the hexagonal phase and investigated the MB photo-degradation efficiency. The results demonstrated that the flower-like ZnO possessed more irregular Zn sites than that of the spindle- and sword-like ZnO, with more naked Zn atoms on the defects which prolong binding of S and N atoms in the MB molecules, promoting the photodegradation reaction. Therefore, relatively lower crystallinity and more defects were responsible for enhanced photo-catalytic activity.

Element doping can lead to a red-shift in ZnO optical absorption edge to lower energies and increase the photocatalytic activity in the visible-light region. Kuriakose et al. successfully prepared Co-doped ZnO nanodisks and nanorods through a facile wet chemical method and enhanced photocatalytic activity was obtained [182]. The enhanced photocatalytic activities were attributed to the combined effects of the high surface area of the ZnO nanodisks and high charge separation efficiency caused by optimal Co doping. Similarly, Rajbongshi et al. comparatively investigated the photocatalytic activity of ZnO nanorods and Co doped ZnO nanorods [183]. The high photocatalytic activity of Co doped ZnO under visible light radiation was ascribed to its lower band gap and associated red-shifted absorption. In addition, Cu-doped ZnO microstructures with a large amount of polar surfaces were produced and used as photo-catalysts to degrade MB and rhodamine B by Pawar et al. [184]. They also demonstrated that the Cu-doped ZnO microstructures showed better photo-degradation properties than the undoped ZnO microstructures. The enhanced performance was ascribed to the existence of (001) polar surfaces, oxygen vacancies, and increased optical absorbance at visible wavelengths. Except for the transition metal doping, noble metal doping was also reported. Han et al. prepared Pd-doped ZnO nanofibers via an electrospinning technique and evaluated their photo-catalytic degradation efficiency of MB [185]. Enhanced photo-catalytic activity was obtained compared to pure ZnO nanofibers, which was attributed to the PdO/ZnO heterostructures and the enhanced surface area. Recently, Faisal et al. successfully synthesized Ce doped ZnO nanorods and evaluated their photonic efficiencies for degradation MB [186]. All Ce doped samples exhibited superior photocatalytic performance than either pure ZnO nanorods or Hombikat UV-100. The authors claimed that the narrow band gap caused by Ce doping contributed to the enhanced photocatalytic activity.

It is broadly accepted that hybrid catalysts will enhance photocatalytic properties in comparison to individual semiconductor catalysts [77,78]. For example, Sun et al. found that the photo-degradation efficiency of MB over ZnO nanorod arrays (NRs) was significantly enhanced by decoration with Au (ZnO/Au composite) [187]. A broader adsorption band, spanned from 500 to 700 nm in the visible light range was observed over ZnO/Au composite which was believed to result from defects, such as donor acceptor pairs, O and/or Zn vacancies, O and/or Zn interstitials, and surface state [188]. Such an energy absorption edge means a potential enhancement of the photo-catalytic properties. During the photo-catalytic process, ZnO NRs serve as the sources of holes and electrons. Firstly, the electron-hole pairs are produced from ZnO NRs by UV irradiation. Then, the photo-excited electrons relax from the conduction band (CB) to the defect level to react with O_2 (electron acceptors) to form the O_2^- superoxide anion radicals; accordingly, the holes in the valence band react with water to form OH^- hydroxyl radicals. Generally, the photo-catalytic property is mainly related to the amount of O_2^- [189]. However, because of the charge recombination process, the electrons that were necessary for the formation of O_2^- will get lost. Fortunately, here, Au NPs can serve as photo-generated electrons sinks and make the Fermi level shift to a more negative potential [190]. Furthermore, the electrons transfer from ZnO to Au on ZnO/Au interface can be detected when the charge equilibration process occurs. This means electron-hole recombination can be suppressed due to the introduction of Au, and therefore, the photo-catalytic activity is enhanced. Thus, the high photo-degradation efficiency was probably due to the high defects concentration and the suppression of the recombination of electron-hole pairs.

A semiconductor is also applied to modifiy the intrinsic semiconductor in order to improve photocatalytic properties [77,78]. Kayaci et al. produced morphologically well defined poly

(acrylonitrile) (PAN) nanofibrous via electronspinning, and then coated it with ZnO through an atomic layer deposition method, which served as crystal seed to grow single crystalline ZnO nanoneedles via a hydrothermal process [191]. The characterization indicated that PAN/ZnO seed samples consist of abundant O^{-x} type ions and grain boundaries, while ZnO needle is a single crystal with less defects and of relatively better optical quality. Compared with PAN/ZnO seed samples, PAN/ZnO nanoneedles displayed much higher photocatalytic activities. It was mainly explained by the fact that an oxygen vacancy lies in the ZnO seed and captures a hole from the CB and hence the photo-generated charge combination process is delayed. Also this captured hole can take part in photocatalytic reactions when it is located within the grain boundary region of PAN/ZnO seed. This collective effect enabled the active participation of defect state and catalysis taking place at CB as well as VB, leading to higher photocatalytic activity. Then, Zhu et al. prepared carbon nanotube (CNT) and hierarchical ZnO microsphere composites (ZnO/CNT) and applied them to photo-catalytic degradation of MB [192]. The results showed that the photocatalytic activity of ZnO/CNTs composites is superior to that of pure ZnO microspheres. The observed photocatalytic performance improvement can be attributed to the triple effects, high surface area, enhanced light absorption, and suppression of charge carrier recombination resulting from the interactions between ZnO and CNT. Moreover, Chang made a comparison of complex ZnO/ZnS nanocable and nanotube arrays [193]. The complex ZnO/ZnS nanocable and nanotube arrays have excellent photocatalytic activities compared to ZnO nanowire arrays. This result is ascribed to the increase of the separation and transfer of photoinduced electrone-hole pairs on the surface of the ZnO/ZnS nanocable and the surface-to-volume ratio on the ZnS nanotube. Considering both ZnO and TiO_2 are widely used in photo-catalysis, both Avci and Wang et al. investigated the photo-catalytic degradation of MB over ZnO-TiO_2 nanocomposites [194,195]. Avci et al. directly and synchronously synthesized a rutile TiO_2 (α-TiO_2) and hexagonal wurtzite ZnO nano-composite via the arc discharge method [194]. Then, α-TiO_2 and hexagonal wurtzite ZnO nano-sphere and nanorod composites were thoroughly investigated. The results indicated that the ZnO-TiO_2 nano-composite catalyst exhibited remarkably superior photo-catalytic properties compared with the pristine ZnO or TiO_2 nanoparticles. The better photo-catalytic properties were ascribed to the suppression of the recombination of electron-hole pairs and the synergetic effects occurring between hexagonal wurtzite ZnO and rutile TiO_2 phases related to ZnO morphology.

3.1.2. Photo-Degradation of Methyl Orange (MO)

MO is another extensively explored organic dye in waste water and ZnO is also widely utilized in its photo-degradation. ZnO nanowires were extensively investigated in the photo-degradation of MO. Liu et al. [196] synthesized ZnO nanowires and directly applied them to MO photo-degradation. A high photo-catalytic activity and stability for MO degradation was obtained and was ascribed to the increased defects of ZnO nanowires. What is more, if the nanowire's diameter is less than the critical value (about 50 nm), the ZnO effective band gap will increase, as the redox potentials; therefore the photo-generated charge carriers will possess higher reducing/oxidizing capabilities. Besides, the recombination of photo-generated charge carriers will be inhibited with the higher band gap. This increases the charge transfer efficiency between the pollutants and the catalyst, leading to a higher catalytic activity under mercury lamp irradiation.

Lu et al. [197] showed that ZnO nanorods can improve photo-catalytic properties of MO degradation. They believed that ZnO nanorods possess higher aspect ratio and larger specific surface area compared with ZnO nanoparticles, which enhance light photon capture efficiency, promote the generation of photo-induced charges and accelerate their transfer rate [198]. The wurtzite crystal structure especially contains a lot of Zn^{2+} and O^{2-} terminated facets which alternately stack along the c axis, thus, ZnO nanorods possess Zn^{2+} terminated (0001) and O^{2-} terminated ($000\bar{1}$) facets [199,200]. Then, a built-in electric field in ZnO nanorods is constructed between the two polar crystal facets, where the transfer path of photo-induced charges is undoubtedly influenced. Meanwhile, it was revealed

that photo-corrosion cracks were generated especially along the c-axis of pristine ZnO nanorods after five photo-degradation cycles. In addition, Li et al. explored the effects of ZnO nanorod diameter size, orientation and surface area on the photo-catalytic activity of MO photo-degradation [201]. ZnO rod arrays with various diameter sizes and orientations were successfully synthesized and evaluated. The results demonstrated that the photo-catalytic activities of ZnO rod arrays enhanced along with the rod diameter size decrease and array orientation increase. Usually, a smaller rod diameter size results in a larger surface area, providing more active sites for an enhanced catalytic activity. As for the orientations, the authors suggested that a high orientation of ZnO arrays could increase the amount of exposed polar facets, leading to enhanced photo-catalytic activity. Thus, ZnO rod arrays with the smallest diameter size and the highest orientations displayed excellent MO photo-catalytic degradation properties. The importance of array orientation was further investigated by the same group later [202]. The high orientation led to an increased quantity of exposed (0001) facet per unit area which suppressed the recombination of photo-generated charges to dominate the photo-catalytic activity of ZnO nanorods. According to previous publications, the electron flow following photo-excited electron-hole pair creation can be directed by coupling metal oxides to match the electrochemical potential of semiconductors. This can not only make ZnO capable of using visible light, but also increase the charge separation and suppress charge carrier recombination, increasing photo-catalytic activities [203,204]. So, Danwittayakul et al. fabricated ZnO nanorods with zinc stannate (ZTO) by direct growth, then coated them with polyester fiber membranes or porous ceramic by a mild hydrothermal method [205]. As expected, ZTO with higher-bandgap (3.6 eV) bounded to lower-band gap ZnO (3.37 eV) triggers the photo-excited electrons transfer from the ZTO conduction band to the ZnO conduction band, while the hydroxyl groups could be kept on the ZTO surface, suppressing the charge recombination (Figure 9). Moreover, the hetero-junctions between ZnO and ZTO formed, also promoting photo-excited electron transfer from ZTO to ZnO and pinning the holes on the ZTO surfaces, then facilitating charge separation, leading to an enhanced photo-catalytic activity. In addition, electrons transfer from ZTO to ZnO nanorods which on one hand enhanced the surface electron density on the surface of ZnO nanorods, promoting photo-reduction reactions; on the other hand possibly leaked to the environment (dye solution), causing dye reduction reactions. Therefore, the engineered structure of CZnO/10ZTO catalyst exhibited good MO photo-degradation properties, degrading around 95% MO within 3 h under UV-light irradiation.

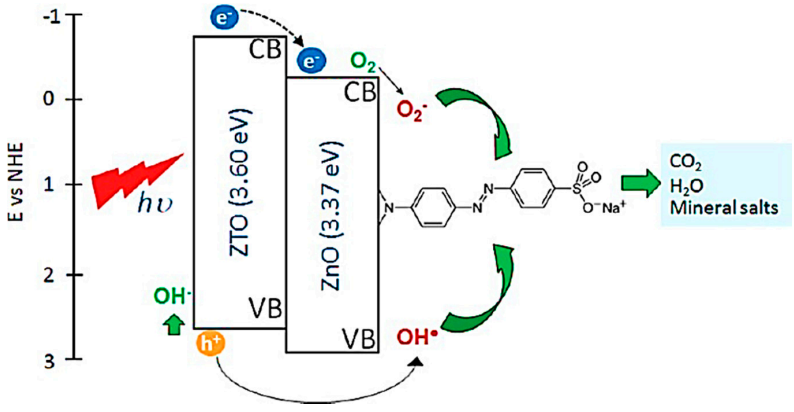

Figure 9. Possible energy band diagram of a ZnO/ZTO nanocomposite showing the photo-excited electron transfer from the higher-energy-level CB of ZTO to the lower CB of ZnO. Reproduced with permission from [205]. Copyright American Chemistry Society, 2013.

Besides ZnO nanorods, two-dimensional ZnO, such as nanofilm and nanosheets, was also prepared for MO degradation. For example, ZnO thin films were successfully synthesized by Gong et al. and tested for photo-degradation properties of MO [206]. The maximum MO degradation efficiency

reached 64.4% after UV-irradiation for 180 min. In their research, the water contact angles of ZnO thin films were detected before and after UV irradiation. The contact angles decreased rapidly after UV irradiation for 120 min which indicated a transition from hydrophobicity to hydrophilicity. The reduction rate of the contact angles was defined as the ratio of the change of respective contact angles after exposure to UV for 120 min to its initial value and it was thought that the smaller the reduction rate, the more obvious the photo-induced hydrophilicity. Generally, it is believed that repellent films will become more hydrophobic, hydrophilic films will be more hydrophilic with lower surface free energy and higher surface roughness. Therefore, the decrease of contact angle values of ZnO thin films may be ascribed to a synergistic effect of decreasing surface roughness and increasing surface free energy. It was also claimed that when the film was irradiated by UV, it will produces electron-hole pairs and when holes react with the lattice oxygen, surface oxygen vacancies are formed. In the meantime, there is a competitive adsorption between oxygen and water for these vacancies. The further kinetic study indicated that hydroxyl adsorption was preferred on the defective sites. Consequently, the surface hydrophilicity was increased and the contact angle was obviously reduced. Thus, the enhanced photo-catalytic activity was ascribed to the decreased diameter size, surface free energy, and surface roughness accompanied to increased oxygen defect density.

Except for two-dimensional ZnO thin films, ZnO with different dimensions like sheets, rods and tubes, were successfully synthesized and their photo-catalytic activities of MO were comparatively investigated [207–210]. For example, Chen et al. intensively studied porous wurtzite ZnO nanosheets and ZnO nanorods [207]. Compared to ZnO nanorods, the porous ZnO nanosheets showed superior photo-reactivity. DFT calculation suggested that there is an internal electric field between the exposed positive Zn-ZnO (001) and negative O-ZnO ($00\bar{1}$) surfaces due to spontaneous polarization, promoting charge separation. Thus, the superior photo-catalytic activity was attributed to exposed (001) facets and a high specific surface area. Similarly, ZnO nanosheets were also prepared by Hong and Xiao et al. who also reported the display of superior photo-catalytic activity with easy separation and reutilization [208,209].

Besides the broadly investigated ZnO morphologies mentioned above, some special 3D morphologies were also explored. For example, Gomez-Solís et al. synthesized nanocorncobs (Figure 10) and tested for MO photo-degradation [211]. Results indicated that the synthesized ZnO showed much higher activity, almost completely degrading MO under solar irradiation for 90 min, much more active than commercial ZnO under similar reaction conditions. This is mainly because the synthesized ZnO nanocorncobs hold a lot of polar planes which are favorable for oxygen vacancy production. Meanwhile, oxygen vacancies could deter photo-corrosion, decrease the recombination of photo-excited charge carriers, and then improve the catalyst chemical stability. Thus, it was concluded that the synergistic effect between oxygen vacancies and ZnO polar planes was responsible for the enhanced catalytic activity. Srikhaow et al. prepared flower-like ZnO and evaluated their photo-degradation properties of MO [212]. This showed rather high photo-degradation efficiency of MO, higher than 85% after irradiation for 45 min. They stated that the high photo-catalyticactivity was led by the large amount of oxygen vacancies and high specific surface area of the material.

Because of the wide investigation of ZnO nanorods, its modification has also attracted great interest. Misra et al. fabricated ZnO with Au by the synthesis of Au@ZnO core–shell nanostructure and evaluated their photodegradation efficiency of MO under visible irradiation [213]. Au@ZnO core-shell nanostructures exhibited efficient plasmonic photocatalytic activity compared with pure ZnO because of the existence of surface plasmon resonance (SPR) in the Au core. What is more, the photocatalytic activity of the Au@ZnO core-shell NPs was found enhanced by the shell thickness. Recently, Lu et al. intensively investigated the effects of Au modification on the photocatalytic activities of MO degradation [197]. They proposed that when the ZnO surface was modified with Au nanoparticles, it was able to effectively prohibit the occurrence of photo-corrosion and enhance its photo-catalytic property because of the Au SPR effects. On one hand, the Au SPR effect could enhance the ability of light absorption and electron capture over Au/ZnO nanorods; on the other hand,

the amount of surface adsorbed hydroxyl groups could be increased. Because Au nanoparticles can trap photo-generated electrons and hydroxyl groups are the favorable hole scavengers, the generation and separation of photo-induced charges are promoted. In short, when ZnO nanorods were modified by Au nanoparticles, the resistance ability to photo-corrosion, light absorption, and the generation and separation of photo-induced charges were all improved. Thus, both the effects of one-dimensional ZnO morphology and noble metal SPR contribute to the high photo-catalytic properties of MO degradation. In addition, element doping is emerging and it has also been applied to modify ZnO nanostructures. For example, Xiao et al. studied the photocatalytic performance of supported Fe doped ZnO nanorods [214]. Fe entered the ZnO lattice, which introduced lots of defects, dislocations, and distortions, resulting in an increased absorption of light and a decreased recombination rate of electron-hole pairs, leading to enhanced photocatalytic performance, compared with undoped ZnO nanorods.

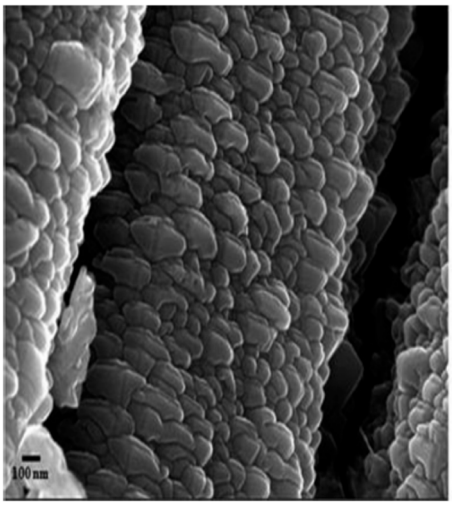

Figure 10. FE-SEM images of ZnO with morphology of nano-corncobs. Reproduced with permission from [211]. Copyright Elsevier, 2015.

Besides, quantum dot (QD) sensitization has been widely used to modify semiconductor catalyst too. Huang et al. assembled QDs, (e.g., CdSe, CdSe/ZnS core-shell) onto ZnO nanorods and applied them to MO photo-catalytic degradation [215]. Compared to the MO reaction solution and pristine ZnO nanorods, CdSe QD-sensitized ZnO nanorods exhibited a stronger light-harvesting capability and much improved photo-catalytic property. The reason is that the CdSe QDs possess a small band gap, therefore expanding its response to the visible light region in the solar spectrum, compared to pristine ZnO nanorods with a large band gap which can only use ultra-viole light. In addition, the band alignment is favorable for the photo-generated electrons and holes separation. Moreover, one-dimensional-ordered ZnO nanorods can offer an unblocked passageway for the charge carrier transportation to reduce their recombination. Compared to the CdSe QD-sensitized ZnO nanorods, the CdSe/ZnS QD-sensitized nanorods presented lower photo-catalytic performance. This is ascribed to the higher charge carrier transfer barrier of ZnS shell layers. In addition, the bottom of the CdSe conduction band is lower than that of ZnS, which implies that the photo-generated holes on CdSe cannot react with H_2O to form hydroxyl radicals or oxidize MO easily. Thus, CdSe QD-sensitized ZnO nanorods presented the best catalytic performance compared with pristine ZnO nanorods and CdSe/ZnS QD-sensitized nanorods.

Except for the modification of semiconductor catalyst to improve photocatalytic performance, the development of special composite strucutures is also very popular. Hierarchical micro/nano architectures have been extensively explored. Lu et al. reported a new ZnO hierarchical micro/nano architecture (Figure 11) fabricated by a facile solvo-thermal approach in an ethylenediamine (EDA)

aqueous solution [216]. This hierarchical core/shell structure is composed of a hexagonal-pyramid-like microcrystal core and a dense nanosheet built network shell. The ZnO hexagonal micro-pyramid has external surfaces that consist of lateral planes ($0\bar{1}11$) and basal planes (0001). The uniform nanosheets are about 10 nm thick and contain a single-crystal structure with ($2\bar{1}\bar{1}0$) sheet-planar planes. This engineered ZnO presented much higher photo-catalytic activities and durability for the photo-degradation of MO compared with other nano-structured ZnO, such as nanosheets, nanoneedles, and nanoparticles. This structured ZnO illustrated a strong structure-induced increase of photo-catalytic performance and the paramount high activity was due to its high ratio of surface-to-volume, which presents a large specific surface area (>180 $m^2 \cdot g^{-1}$) and stability against aggregation. Later, Lu et al. synthesized hierarchical ZnO microarchitectures assembled by ultrathin nanosheets and studied their photocatalytic performance [217]. This hierarchically-structured ZnO displayed a strong structure-induced enhancement of photocatalytic performance which was also ascribed to the large specific surface areas and high proportion of active polar (0001) facets. Besides the development of hierarchical architectures, heterojunctions have also been intensively developed. For example, Lin et al. successfully fabricated Shell@core-nanostructured TiO_2@ZnO *n-p-n* heterojunction nanorods and evaluated their photodegrading performance of MB [218]. The photocatalytic performance increased three times compared with that of wurtzite hexagonal ZnO which was ascribed to the driving force of the inner electric field, efficiently promoting the separation and transfer of photogenerated electron-hole pairs. Similarly, Yi et al. obtained novel heterojunctions of p-type BiOBr and *n*-type ZnO by loading amounts of BiOBr nanoflakes onto the surface of ZnO nanoflowers [219]. The decolorization rate of BiOBr-ZnO heterojunctions was found to be 3.7 and 4.7 times higher than that of pure BiOBr and ZnO, respectively.

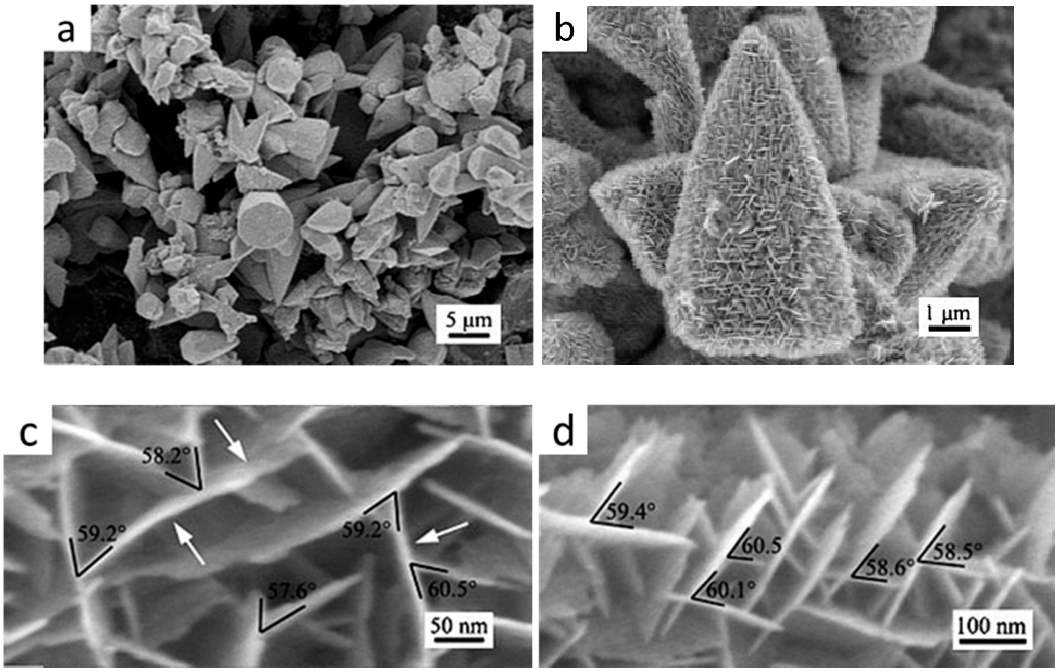

Figure 11. FE-SEM images of the products prepared by the solvothermal reaction. (**a**) A general-view image; (**b**) The local magnification image of (**a**); (**c**) A further enlarged top-view image of (**b**); (**d**) Enlarged local image at the edge of the networks. Reproduced with permission from [216]. Copyright WILEY-CVH, 2008.

3.1.3. Photo-Degradation of Rhodamine B (RhB)

ZnO structures with different morphologies (nanosheets and nanorods) and percentages of polar facets were synthesized through a two-step chemical bath deposition process under mild

conditions [220]. The ratio of ZnO polar facets could be finely controlled by utilization of Bi_2WO_6 as crystal seeds and the prepared ZnO nano-structures were tested for photo-degradation properties of RhB. The photo-catalytic activity was enhanced over ZnO nano-structures with a higher ratio of polar facets. The fraction of polar facets increased with the increase of the Bi_2WO_6 mass ratio which led to a more efficient separation efficiency of photo-generated charge carriers or a longer lifetime of the photo-excited electron-hole pairs, enhancing the photo-degradation efficiency of RhB. Later, Wang et al. successfully synthesized defect-rich ZnO nanosheets with high surface area and investigated the photo degradation performance of RhB under visible-light illumination ($\lambda > 420$ nm) [221]. The ZnO nanosheet with rich oxygen-vacancies exhibited enhanced photocatalytic activities, about 11 times higher than that of ZnO nanoparticles with few oxygen-vacancies. Moreover, when hybridized with Ag_3PO_4 nanoparticles, the hybride catalyst displayed even higher visible-light photocatalytic performance. The authors claimed that high surface area contributed to the increased surface oxygen-vacancies, which could improve the visible-light absorption and act as active sites for photocatalytic reactions. In addition, the hybridization favored the efficient charge transfer between ZnO and Ag_3PO_4 through energy level matching, suggesting a synergistic effect of surface oxygen vacancies and Ag_3PO_4 coupling. In order to achieve high surface area, 3D ZnO morphologies such as flower-like were investigated [222–224]. For example, Li et al. successfully synthesized ZnO micro-flower arrays, micro-candles, and micro-rods and explored their photo-degradation properties of RhB [223]. As for the results, ZnO micro-flower structures demonstrated superior photo-catalytic properties for RhB degradation although it lacked (0001) facets in its partial hollow structures, compared with micro-rods and micro-candles. However, it owned a high surface area which could promote organic dye adsorption and higher oxygen vacancies density, serving as an electron capturing center. In addition, Lu comparatively investigated the photodegradation efficiency of RhB over plate- and flower-like ZnO nanostructures [224]. The results demonstrated that flower-like ZnO was more efficient for RB photodegradation than plate-like ZnO. The high efficiency of flower-like ZnO was due to its more efficient separation and transfer properties of photogenerated charges than that of plate-like ZnO, originated from the special flower-like hierarchical nanostructures.

Hierarchically structured and heterostructure composite are usually responsible for the high photocatalytic performance [225–230]. For example, the flower-like ZnO hierarchical microstructures assembled by interleaving nanosheets were prepared and tested for photodegradation of RB [225]. The results indicated that the flower-like ZnO sample showed an enhanced photocatalytic performance, compared to ZnO nanoparticles, nanosheets, and nanorods. The high photocatalytic performance can be attributed to its open and porous nanostructured surface layer which significantly facilitates the diffusion and mass transportation of RhB molecules and oxygen species. Besides, hierarchical heteroassemblies, consisting of Ag core nanowires (NWs) covered by ZnO branched nanorods (ZnO BNRs), were successfully prepared and evaluated for the photo-degradation of RhB [227]. The obtained heteroassemblies of Ag NWs-ZnO BNRs exhibited high photocatalytic properties, because of the decisive roles of the synergistic effect of the hierarchical morphologies and the unique metal-semiconductor heterojunction as well as the presence of the dominant (001) surface of ZnO BNRs. In addition, the ZnO nanorods/ZnSe heteronanostructure arrays were also reported to exhibit enhanced photocatalytic activities due to their special heteronanostructures [229].

In order to increase photocatalytic activities, many efforts have been made to prepare element doped ZnO [231–236]. Main group metals, transition metals, and rare-earth metals are all reported in preparing doped ZnO [231–236]. Very recently, Li et al. made Ga doped ZnO photonic crystals (GZO PCs) with various pore diameters and utilized them for RhB degradation [231]. The high photocatalytic activity was ascribed to the slow photon effect from the photonic crystal structure and increased specific surface area after Ga doping. Furthermore, both transition metal Ni-doped ZnO hierarchical hollow nanospheres and Ni-doped-ZnO@void@SiO_2 core-shell nanocomposite were reported by Yin group [232,233]. The high photocatalytic activity of Ni-doped ZnO hollow nanospheres was attributed to the high fraction of exposed polar facets, smaller particle size and larger surface

area [232]. In addition, ZnO with different morphologies doped by rare-earth metals such as Ce and Eu were also explored [234,235]. The excellent photocatalytic activity for the degradation of RhB was attributed to crystallite size, narrowed band gap, and oxygen vacancies. Except for single element doping, N-decorated and Mn^{2+} doped ZnO nanofibers were synthesized by Wang et al. [236]. This nanocatalyst exhibited 50 times higher photocatalytic activity for degradation of RhB than that of pure ZnO. This impressive visible-light catalytic activity was ascribed to the huge band gap decrease, originating from the synergetic effects of both Mn^{2+} doping and N decoration, which significantly enhanced the absorption of ZnO nanofibers in the range of visible-light.

3.1.4. Photo-Degradation of Other Organic Dyes

ZnO nanomaterials have been widely used in the photo-degradation of organic dyes, including relatively rare organic dyes, such as Reactive Yellow 15, Orange G etc. [237–247]. Hafez. prepared rod-like ZnO with pointed-shape ends and studied the photo-degradation properties of Reactive Yellow 15, an industrial textile dye [238]. The dye removal efficiency was around 85.7%. This type of ZnO nanorods possesses higher visible light harvesting efficiency compared with other reported morphologies. Besides, in the visible light region, the as-prepared ZnO nanorods displayed two broad emission bands at 486 nm and 564 nm. This intensive green-red luminescence was primarily attributed to the ionized oxygen vacancies, which originated from the recombination of a photon-generated hole at the oxygen-hole vacancy with the single ionized charged state of the defect in ZnO. This confirms the existence of ionized oxygen vacancies which usually promote photo-catalytic reactions. This means that this type of ZnO nanorods benefits the adsorption of oxygen to generate oxygen interstitials defects, due to its porous surface. Thus, the high photo-degradation efficiency was mostly ascribed to the formation of a large number of oxygen defects. Interestingly, Leelavathi et al. investigated the photo-degradation properties of Orange G over ZnO nanorods with different aspect ratios and high aspect ratio ZnO nanorods largely bound by the prism planes [239]. The high aspect ratio rods exhibited significantly high visible light photocatalytic activities compared with the low aspect ratio ZnO nanostructures. It was attributed to the easy separation of photogenerated charge carriers in the high aspect-ratio structures and the presence of favourable sites on the prism planes which contribute to enhanced oxygen chemisorption, and then promote the production of reactive radicals.

Generally, porous ZnO nanostructures can increase the specific surface area and lead to high catalytic activities. Different, kinds of porous ZnO nanostructures have been developed and applied to organic dye removal [240–244]. Srinivasan et al. prepared various mesoporous morphologies of ZnO (Figure 12), i.e., square bipyramid, bicone, radially oriented nanorod and sphere, and evaluated their Crystal Violet dye photo-degradation performance under UV-B and UV-C irradiation [240]. Although the sphere possessed the highest surface area (77.6 m^2/g), it exhibited the lowest catalytic activity compared with radially oriented nanorod (58.1 m^2/g), bicone (12.3 m^2/g), and square bipyramid. Under both investigated irradiation sources, square bipyramid had the highest photo-catalytic activity due to its higher crystallinity. In addition, under UV-B irradiation, radially oriented nanorod showed a comparable photo-catalytic activity to square bipyramid; however, under UV-C irradiation, it showed lower activity. Therefore, under UV-B irradiation, both radially oriented nanorod and square bipyramid possess the highest degradation rates and rate constants; under UV-C irradiation, only square bipyramid still gives the highest degradation rates and rate constants. The good photo-catalytic performance of radially oriented nanorod was due to its special morphology and its rich meso-porous structure which can stimulate the adsorption of organic dye molecules. Thus, the authors proposed that both accessible meso-porous structure and high crystallinity are essential to the high photo-catalytic efficiency.

Various hierarchical hollow structured ZnO materials were also successfully synthesized for photodegradation of organic dyes [241–244]. Lan et al. evaluated the photo-degradation properties of Congo Red (CR) over hierarchical hollow structured ZnO [241]. The data demonstrated that the morphology controlled ZnO exhibited higher adsorption ability and photo-catalytic property

than those of commercial ZnO and TiO_2 P25. These excellent properties were due to the porous structures causing large surface area, which obviously promoted the diffusion and mass transportation of dye molecules and delayed the electron-hole pairs' recombination during the photo-catalysis process. Metal or metal salt modified hierarchical hollow structured ZnO materials were developed for photodegradation of organic dyes too [243,244]. For example, Yu et al. explored the degradation of Orange II over novel hollow Pt-ZnO nanocomposite microspheres [243]. The enhanced photocatalytic activity and stability were due to the following reasons: first, the unique hierarchical nanostructures will lead to high light collection efficiency and a fast motion of charge carriers; second, the specific structures of Pt-ZnO nanocomposite microspheres can effectiently promote the transportation of the reactant molecules to the active sites on the framework walls. Similarly, Lamba et al. fabricated hierarchical cauliflower-like AgCl/ZnO nanocomposite, self-assembled by 1D-nanorods, and used it for malachite green (MG) photo-catalytic degradation [244]. The as-synthesized cauliflower-like nanocomposite exhibited remarkable high photocatalytic activities under visible light. The excellent catalytic performance was ascribed to the effectively extended absorption edge into the visible region, efficient electron-hole separation, and strong adsorption capability, originating from the special AgCl/ZnO hierarchical nanostructures.

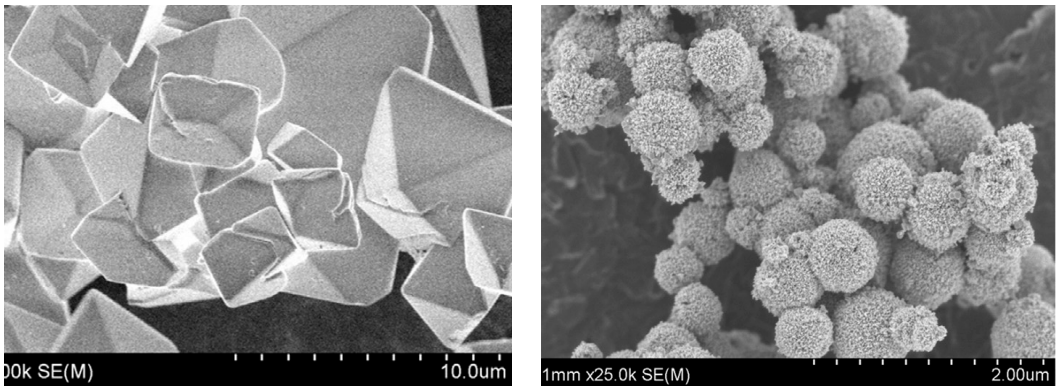

(**a**) (**b**)

Figure 12. SEM image of bicone ZnO (**a**) and spherical ZnO (**b**). Reproduced with permission from [240]. Copyright Elsevier, 2008.

Besides, various morphologies of semiconductor-ZnO nanocomposites and element doped ZnO were also synthesized and applied to the photo-degradation of organic dye molecules [245–247]. Lamba et al. prepared well-crystalline CeO_2-ZnO hexagonal nanodisk composites and evaluated their photo-degradation performance of Direct Blue 15 (DB-15) dye under solar light irradiation [245]. The possible DB-15 dye photo-degradation mechanism on CeO_2-ZnO nano-composite can be demonstrated as follows (Figure 13). VB and CB of ZnO are below that of CeO_2, under solar light irradiation, the photo-generated electrons from CB of CeO_2 are transferred to the CB of ZnO where they reduce the adsorbed O_2 to form super reactive radical anions, $O_2 \cdot^-$. Then, $O_2 \cdot^-$ combines with an electron to produce H_2O_2. Accordingly, the photo-generated holes are transferred from the VB of ZnO to the VB of CeO_2 where they oxidize OH^- to ·OH. These in-situ produced ·OH radicals enable the complete degradation of DB 15-dye. Therefore, electron-hole pair recombination was inhibited, resulting in an enhanced photo-catalytic activity. In addition, Cu-doped ZnO nanorods with different Cu concentrations were synthesized by Mohan et al. who tested their resazurin (Rz) dye photo-degradation performance [246]. The results demonstrated that ZnO nanorods with increasing Cu doping exhibit enhanced photocatalytic activity. It was chiefly because the surface defects caused by Cu doping could serve as favorable trap sites of the electrons or holes, suppressing their recombination and consequently increasing their photocatalytic activities. In addition, a bigger surface to volume ratio of nanorods, results in more surface oxygen vacancies and thus also increased surface activity. Similarly,

Cu-doped ZnO with hexagonal prism-shape was also reported to photodegrade Acid Orange 7 by Wan et al. [247]. The excellent photo-catalytic activity was ascribed to the presence of more defects and weaker PL emission, induced by Cu doping which also led to the change of ZnO morphology. What is more, the amount of highly active (0001) facets and surface roughness were also thought to increase the catalyst properties.

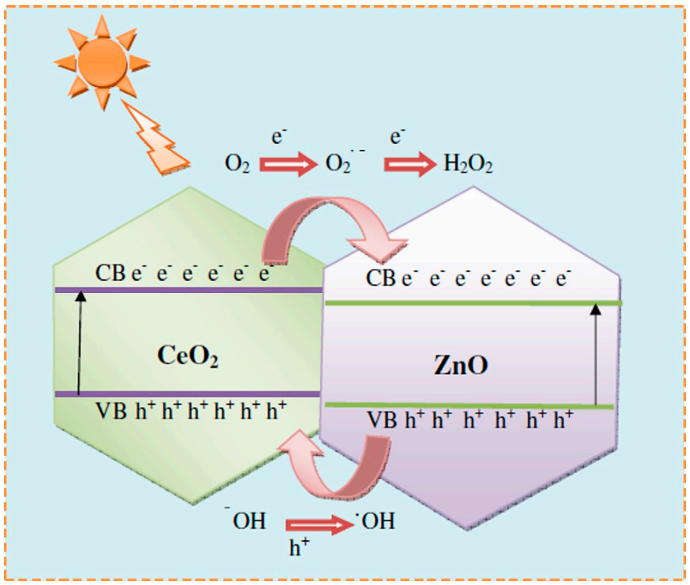

Figure 13. Proposed schematic illustration of photocatalytic activity of the prepared CeO_2-ZnO hexagonal nanodisk photocatalyst under solar light irradiation. Reproduced with permission from [245]. Copyright Elsevier, 2015.

3.2. Photo-Degradation of Phenol and other Pollutants

Apart from the degradation of the dyes mentioned above, phenol degradation was also broadly investigated. Xu et al. synthesized ZnO hexagonal nanoplate single-crystalline in a surfactant-free system and used it for photo-degradation of phenol [248]. An enhanced photo-decomposition activity of phenol compared with ZnO powders was obtained and it was ascribed to the unique surface nano-features with high ratio of polar facets and high concentration of defects. Besides, well-built 2-dimentional nanostructures with boundaries on nanoplates are favorable for advanced optical properties and enhanced photo-catalytic properties. Porous ZnO nanosheets with a high surface area near-rectangular morphology have been successfully prepared by Liu et al. [249]. The samples showed good activities for photo-degradation of phenol under UV light irradiation. It is because the large specific surface area can provide more active sites for the reaction and then facilitate the diffusion and mass transportation of the pollutants and hydroxyl radicals during the photochemical reaction. In addition, the surface defects may serve as charge carrier traps as well as adsorption sites where the charge transfers to the adsorbed species and prevents electron-hole recombination, whereas bulk defects only act as charge carrier traps where electron-holes recombine in the photocatalytic process. Thus, large surface area induced defects also contributed to the high catalytic activity.

The applications of various morphologies of ZnO to phenol photodegration have been intensively comparatively studied [14,250,251]. Xu et al. investigated photo-degradation properties of phenol over various morphologies of ZnO such as spherical particles, rod, tubular, hourglass, truncated hexagonal conical, and cauliflower [14]. Cauliflower ZnO illustrated the highest catalytic properties whose kinetic rate constant k was 0.1496 min^{-1}. This was 9-times higher compared to commercial ZnO. However, no relationship between the catalytic activity and surface area was found. The main reason for the increased catalytic performance was ascribed to morphology effects. Interior cavities

were found in conical ZnO and it was claimed that multiple reflection of UV light within the interior cavities could take place, which allowed for the high efficient use of the incident light, leading to an improved catalytic performance. Besides, the synthesized ZnO with more low energy facets was observed to possess a decreased photo-catalytic activity. Furthermore, the differences in the concentration and type of oxygen vacancies were also confirmed to result in different photo-catalytic activity. Similarly, Selvam et al. synthesized ZnO nanoflakes, nanorods and spherical nanoparticles (SNPs), and applied them to phenol photo-degradation [250]. Spherical ZnO nanoparticles illustrated enhanced photo-catalytic performance in comparison with the other morphologies of ZnO, which was owing to the narrow crystal size distribution, high specific surface area, and high concentration of oxygen vacancies. Rezapour et al. also synthesized various morphologies of highly crystalline ZnO and investigated their photo-degradation properties of phenol [251]. ZnO structures with spherical, well-faceted hexagonal, agglomerated particles and nearly hexagonal rods were synthesized by a solvo-thermal synthesis method, using ethylene glycol, ethanol, PEG 600, and 1,4-butanediol as solvent, respectively. Nearly spherical particles and squares were prepared via sol-gel synthesis, by using ethanol and other solvents, respectively. The ZnO obtained by both methods using ethanol as the solvent exhibited the best photo-catalytic performance. Besides, the sol-gel synthesized ZnO samples illustrated an improved photo-catalytic property toward photo-degradation of phenol compared to those prepared using the solvo-thermal method. For details, when the size of the ZnO nanosphere is smaller than the critical radius, a series of discrete electronic states will be created through an effect of charge confinement. Consequently, the effective band gap will increase and a band edge shift will occur. So, as the particle size decreases, the transfer of photo-induced electrons or holes from bulk to surface will be accelerated, leading to an enhanced photo-catalytic activity. What is more, the smaller dimension of ZnO spherical nanoparticles were proved to contain more surface defects which on one hand could enhance the number of surface active sites, and on the other hand could serve as electron traps to suppress the recombination of photo-generated charge carriers. Meanwhile, polar planes possess high surface energy and promote the adsorption of OH^- ions and oxygen molecules, leading to a higher generation rate of OH· radicals and H_2O_2. Therefore, the high photo-catalytic activity also arose from the narrow particle size distribution, high specific surface area, high ratio of polar planes, and high concentration of surface defects.

Besides pristine ZnO with various morphologies, ZnO based composites including special structures were also prepared and tested for the photo-degradation of phenol [252–254]. Lama et al. synthesized Nb_2O_5/ZnO nanorod composites and tested their photo-catalytic activity [252]. The superior photocatalytic activity of the Nb_2O_5/ZnO NRs was attributed to the extended light absorption region and high fast charge transfer rate, caused by the incorporation of Nb_2O_5 into ZnO. Similarly, metal oxide-ZnO nanorod composites were prepared via a green surfactant-free hydrothermal approach by Lam et al. and applied to phenol photo-degradation under UV irradiation [253]. Under similar conditions, phenol was completely photo-degraded in the presence of Nb_2O_5/ZnO and Cr_2O_3/ZnO nano-composites under irradiation for 60 and 90 min, respectively. The results indicated that these composites displayed superior photo-catalytic properties in comparison with the commercial TiO_2. The enhanced photo-catalytic property was ascribed to the lower band gap of rod-like ZnO. Furthermore, some special structured ZnO composites were also investigated. For example, Wu et al. successfully prepared ZnO/ZnMgAl-CO_3-LDHs (layered double hydroxides) hetero-junction and explored their photo-degradation properties of phenol [254]. The hetero-junction photo-catalyst showed better photo-catalytic performance than neat ZnMgAl-CO_3-LDHs microspheres and pure ZnO under UV light irradiation. This result can be ascribed to the inhibition of the recombination of the photo-excited electron-hole pairs caused by the hetero-junction structure, small size of ZnO, and improved light absorption properties.

Various morphologies of ZnO nanomaterials undoped or doped with transition metal or rare earth metal were reported for photodegradation of phenol, 2,4-dichlorophenol (2,4-DCP), and 2-chlorophenol etc, especially by Sin et al. [255–261]. Sm-doped ZnO nanorods and rare earth metal (Eu-, Ce-, Sm-)

doped ZnO hierarchical micro/nanospheres were all successfully prepared for the photodegradation of phenol and 2,4-DCP [255–259]. The enhanced photocatalytic performance was attributed to the narrow band gap, high charge separation efficiency, and high hydroxyl radical generation ability, induced by rare earth metal doping. ZnO nanorods have been used to photo-catalyze the aerobic oxidation of alcohols to aldehydes under ambient conditions by Tang et al. [261]. ZnO nanorods demonstrated a markedly enhanced photoactivity and selectivity compared to commercial ZnO. This was ascribed to the efficient separation of photo-generated chargecarriers and its favorable, selective absorption toward the reactant of alcohols rather than the product of aldehydes, induced by the special 1D morphology of ZnO nanorods.

Except for the photodegradation of organic dyes and pollutants, some other inorganic pollutants were also photodegradaded by morphology controlled ZnO [262]. For example, grapheneoxide (GO) was used to tune the morphologies of ZnO and their photo-activity of the reduction of Cr(VI) under visible light irradiation [262]. The oxygenated functional groups and the unique structures of 2D GO played pivotal roles in tuning the morphology of ZnO and increasing oxygen vacancies concentration. In addition, the introduction of oxygen vacancies and the intimate interfacial interaction between ZnO and reduced grapheneoxide (RGO) extended the light absorption edge of RGO-ZnO to the visible light region. Thus, the RGO-ZnO nanocomposite exhibited enhanced visible light photo-catalytic activity toward the reduction of heavy metal ions Cr(VI).

For photo-catalysis, the morphology effects of ZnO have been summarized as shown in Table 2; the corresponding promotion mechanisms have been proposed in Figure 14 and as follows:

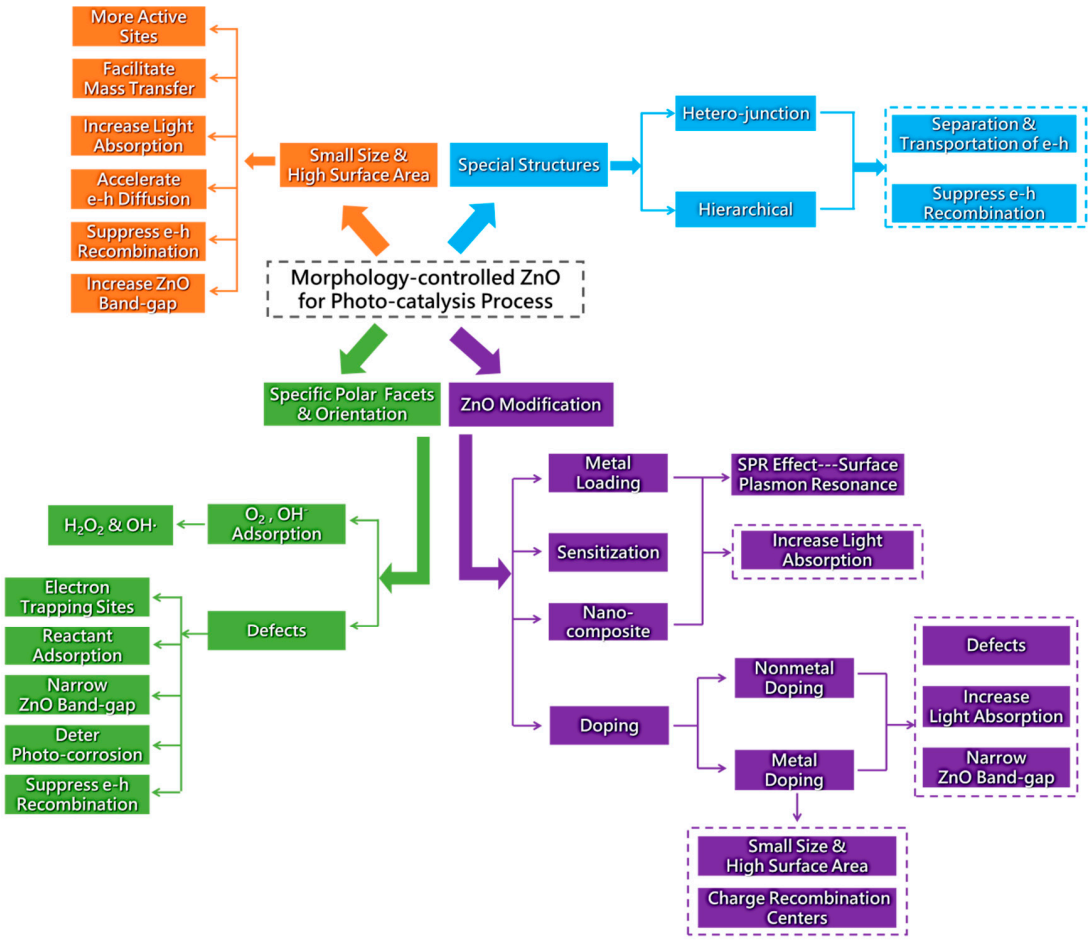

Figure 14. Promotion mechanism illustration of morphology controlled ZnO in photo-catalysis.

Table 2. The applications of morphology controlled ZnO in the photo-catalytic process.

Type of Catalytic Reactions	Catalyst	ZnO Morphology	Morphology-Dependent Promotion Mechanisms	Reference
Degradation of Methyl blue	ZnO	Nanorods, hexagonal plate	The hexagonal ZnO QDs have more polar O-terminated $(00\bar{1})$ and Zn-terminated (001) facets which are facile to the adsorption of oxygen molecules and OH^- ions, leading to higher generation rate of H_2O_2 and ·OH radicals, more active for photo-catalysis than the non-polar surfaces on hexagonal rods.	[170,171]
	ZnO	Hexagonal prisms, plates and rose-like twinned crystal films	High percentage of polar facets and concentration of oxygen vacancies.	[172]
	ZnO	Nanorods, nanoplates	ZnO rods were more active for the decomposition of MB and phenol, the production of ·OH radicals and the generation of photocurrents, all of which were associated with single-electron transfer reactions. ZnO nanoplates were more effective for the production of molecular hydrogen and hydrogen peroxide, both of which are initiated by two-electron transfer reactions.	[179]
	ZnO	Flower-like interwoven grown nanosheets, un-aggregated nanosheets	The oxygen vacancies not only act as the active centers or trap centers for photo-induced charges but also narrow the bandgap of ZnO by the broadening of the valance band.	[180]
	ZnO	Flower-like, Spindle-like, sword-like an dumbella-like	The flower-like structures possessed more irregular Zn sites than that of the other ZnO structures, so more naked Zn atoms on the defects prolong the binding of S and N atoms in the MB molecules, promoting photodegration reactions. Therefore, a relatively lower crystallinity and more defects were responsible for the enhanced photo-catalytic activity.	[181]
	Co-ZnO (doping)	Nanorods	The high visible light activity of Co-ZnO was ascribed to its reduced band gap and associated red-shifted absorption.	[182,183]
	Cu-ZnO (doping)	Rod-like, disk sphere-like	The existence of (001) polar surfaces, oxygen vacancies, and increased optical absorbance at visible wavelengths	[184]
	Pd-ZnO (doping)	Nanofiber	The PdO/ZnO heterostructures and the increase of the surface area	[185]
	ZnO/Au (doping)	Nanorods	The high photo-degradation efficiency was probably due to a broader adsorption band that was caused by discrepancies, such as O vacancies, Zn vacancies, Zn interstitials, O interstitials, donor acceptor pairs, and surface state.	[187]
	ZnO-CNT	Microsphere	The high surface area, enhanced light absorption, and suppression of charge carrier recombination originated from the interaction between ZnO and CNT	[192]
	ZnO- ZnS	Nanocable nanotube	The increased separation and transfer rate of photo-induced electrone-hole pairs on the surface of ZnO/ZnS nanocable and the high surface-to-volume ratio	[193]
	TiO_2-ZnO	Nano-spheres, nanorods	The suppression of electron-hole pair recombination and the synergetic effects between hexagonal wurtzite ZnO and rutile TiO_2 phases that related to ZnO morphology	[194]

Table 2. *Cont.*

Type of Catalytic Reactions	Catalyst	ZnO Morphology	Morphology-Dependent Promotion Mechanisms	Reference
Degradation of Methyl orange	ZnO	Nanowires	The formation of oxygen vacancies; the decreased ZnO nanowire diameter size could increase the effective band gap then the photo-generated electrons and holes have a higher reducing/oxidizing power.	[196]
	ZnO	Nanorods	The higher aspect ratio and larger specific surface area will enhance light photon capture efficiency, promote the generation of photo-induced charges and accelerate their transferrate.	[197]
	ZnO	Nanorod arrays	The smaller particle size could lead to a large surface area, providing more active sites; a high orientation of ZnO arrays could increase the polar facet exposing, leading to an enhanced photo-catalytic activity.	[201]
	ZnO	Nanorod arrays	The high orientation led to the increased quantity of exposed (0001) facet per unit area which decreased the recombination of photo-generated electron-hole pairs.	[202]
	ZnO/ZTO coating polyester fiber membranes orporous ceramic substrates	Nanorods	The coupling of metal oxides to match the electrochemical potential of semiconductors to direct the electron flow following photo-generated electron-hole pair creation enhances the photo-catalytic activity.	[205]
	ZnO	Nanofilms	The influence of morphologies on water contact angles before and after UV irradiation which will alter the ZnO hydrophilicity; when the film is irradiated by UV, it will produce electron-hole pairs. Surface oxygen vacancies are formed when some holes react with the lattice oxygen.	[206]
	ZnO	Nanosheets	The superior photocatalytic activity was attributed to the exposed (0001) facets and a high specific surface area.	[207]
	ZnO	Nano-corncobs	ZnO nano-corncobs hold a lot of polar planes and the polar planes are favorable for oxygen vacancy production which could deter photo corrosion, decrease the recombination of electron-hole pairs and then improve the catalyst chemical stability.	[211]
	ZnO	Flower-like	The high specific surface area and the number of oxygen vacancies in materials.	[212]
	ZnO, ZnO/Au	Nanorods	Both noble metal nanoparticles' SPR effect and one-dimensional ZnO nanostructures' morphology-dependent effects contribute to the high photo-catalytic properties of MO degradation.	[197]
	CdSe and core-shell CdSe/ZnS modified ZnO	Nanorods	CdSe QD-sensitized ZnO nanorods with stronger light-harvesting capability exhibited much improved photo-catalytic performance due to its relatively small band gap. ZnO assembled with core-shell CdSe/ZnS shows lower photo-catalytic ability due to the higher carrier transport barrier originated from ZnS shell layers.	[215]
	ZnO	Nano-sheet built networks on a hexagonal-pyramid-like microcrystal	The external surfaces that consistof a basal plane (0001) and lateral planes ($0\bar{1}11$) present a strong enhancement of photocatalytic performance.	[216]
	ZnO	Nanosheets	The large specific surface areas and high proportion of active polar (0001) facets.	[217]
	TiO_2@ZnO	Shell@core-nanostructured TiO_2@ZnO n-p-n heterojunction	The driving force of inner electric field, efficiently promoting the separation and transfer of photo generated electron-hole pairs.	[218]
	BiOBr–ZnO	Flower-like	The effective separation and transfer of photo-generated charges are responsible for an improved photocatalytic performance due to the existence of the interfacial electric field located between BiOBr and ZnO.	[219]

Table 2. *Cont.*

Type of Catalytic Reactions	Catalyst	ZnO Morphology	Morphology-Dependent Promotion Mechanisms	Reference
Degradation of Rhodamine B	ZnO	Nanorods, nanosheets	The high ratio of ZnO polar facets will lead to a longer lifetime of the photo-generated charge carriers or a more efficient separation of the photo-excited electron-hole pairs, enhancing the high photo-degradation efficiency	[220]
	ZnO	Nanosheets	A higher surface area that increases surface oxygen vacancies to improve the visible-light absorption and act as active sites for photocatalytic reactions. A synergistic effect of surface oxygen vacancies and Ag_3PO_4 coupling; efficient charge transfer between ZnO and Ag_3PO_4 through energy level matching that leads to hybridization property.	[221]
	ZnO	Micro-flower arrays	The high surface area can promote organic dye adsorption and enhance oxygen vacancies density which serve as the electron capturing center; More efficient separation and transfer properties of photogenerated charges	[223,224]
	ZnO	Flower-like hierarchical	The open and porous nanostructured surface layer which significantly facilitates the diffusion and mass transportation of RhB molecules and oxygen species.	[225]
	Ag-ZnO	ZnO branched nanorods	The decisive roles of the synergistic effect of the hierarchical morphologies and the unique metal-semiconductor heterojunction as well as the presence of the dominant (001) surface of ZnO BNRs.	[227]
	Ga-ZnO (doping)	Porous	The slow photon effect from the photonic crystal structure and increased specific surface area after Ga doping	[231]
	Ni-ZnO (doping)	Nanosphere	Higher fraction of exposed polar facets, smaller particle size, and larger surface area.	[232]
	Ce-ZnO (doping)	Nanoflowers	The hierarchical ZnO microflowers ensured a large specific surface area which is favorable for enhancing the light absorption and light propagation. Ce-doped ZnO microflowers illustrated a noticeable red-shift in the absorption band in the visible light region allowing visible light absorption.	[234]
	Eu^{3+}-ZnO	Lotus leaf, cabbage leaf, mushroom-like	The excellent photocatalytic activity and stability for the degradation of RhB (94%) under sunlight was attributed to the crystallite size, band gap, oxygen vacancies, and morphology.	[235]
	N/Mn^{2+}-ZnO (codoping)	Nanofibers	The huge band gap decrease, originated from the synergetic effects of both Mn^{2+} doping and N decoration, which significantly enhanced the absorption of ZnO nanofibers in the range of visible-light.	
Degradation of Yellow GR	ZnO	Nanorods	ZnO nanorods have higher visible light harvesting efficiency and oxygen vacancies which are favorable for photo-catalytic reactions.	[238]
Degradation of Orange G	ZnO	Nanorods	The easy separation of photogenerated charge carriers in the higher aspect-ratio structures and the presence of favourable sites on the prism planes which contribute to enhanced oxygen chemisorption, and then promote production of reactive radicals.	[239]
Degaradation of Crystal violet	ZnO	Square-bipyramid, bicones and spheres	Both high crystallinity and accessible meso-porous structure (high surface area) are essential for high photo-catalytic efficiency.	[240]
Degradation of Congo Red	ZnO	Hierarchical hollow structure	The large surface area and porous structures, which significantly facilitates diffusion and mass transportation of CR molecules and delays the recombination of photo-generated electron-hole pairs in the photo-catalysis process.	[241]

Table 2. *Cont.*

Type of Catalytic Reactions	Catalyst	ZnO Morphology	Morphology-Dependent Promotion Mechanisms	Reference
Degradation of Orange II	Pt-ZnO	Microspheres	The unique hierarchical nanostructures will lead to high light collection efficiency and a fast motion of charge carriers. At the same time, these specific structures can allow more effective transport for the reactant molecules to reach the active sites on the framework walls, hence enhancing the efficiency of photocatalysis.	[243]
Degradation of Malachite Green	AgCl-ZnO	Cauliflower-like	The excellent catalytic performance was ascribed to the effectively extended absorption edge into the visible region, efficient electron–hole separation and strong adsorption capability, originating from the special AgCl/ZnO hierarchical nanostructures.	[244]
Degradation of Direct Blue DB-15	CeO_2-ZnO composite	Hexagonal nano-disk	Under solar light irradiation, the photo-generated electrons from CB of CeO_2 transferred to the CB of ZnO, the photo-generated holes transferred from the VB of ZnO to the VB of CeO_2. Thus, the recombination of the electron-hole pairs is prevented and H_2O_2 and ·OH radicals are produced, leading to enhanced photo-catalytic efficiency.	[245]
Degradation of Resazurin	Cu-ZnO (doping)	Nanorods	The surface defects caused by Cu doping could serve as favorable trap sites of the electrons or holes, suppressing their recombination and consequently increasing their photocatalytic activities. The bigger surface to volume ratio in nanorods, results in more surface oxygen vacancies and thus also increased surface activity.	[246]
Acid Orange 7	Cu-ZnO (doping)	Prism-like	More defects and weaker PL emission introduced by Cu doping which also lead to the changing of ZnO morphology. The amount of high active (0001) planes and surface roughness were also thought to increase the catalysts property.	[247]
Degradation of Phenol	ZnO	Hexagonal nano-plates	The unique surface nanofeatures with high ratio of polar facets, high concentration of defects and the well-built 2-dimentional nanostructures containing boundaries on plates are desirable for the enhanced photo-catalytic properties.	[248]
	ZnO	Nanosheets	A large specific surface area can provide more active sites for the reaction and then facilitates the diffusion and mass transportation of the pollutants and hydroxyl radicals during the photochemical reactions.	[249]
	ZnO	Cauliflower, truncated hexagonal conical, tubular, rod, hourglass and spherical particles	The interior cavities were found in conical ZnO and multiple reflection of UV light within the interior cavities could occur, which allowed for the more efficient use of the incident light, leading to an improved catalytic activity.	[14]
	ZnO	Nano-flakes, nano-rods and spherical nanoparticles	The narrow crystal size distribution, high surface area, and greater amount of oxygen vacancies lead to an enhanced catalytic activity.	[250]
	ZnO	Well-faceted hexagonal, spherical, particles and nearly hexagonal rods	The high photo-catalytic activity arose from the narrow particle size distribution, high surface area, and high ratio of polar planes and increased the concentration of surface defects.	[251]
	Nb_2O_5/ZnO, Cr_2O_3/ZnO composites	Nanorods	The extended light absorption region and fast charge transfer rate, caused by the incorporation of Nb_2O_5 into ZnO.	[252,253]
	ZnO/ZnMgAl-CO_3-LDHs	Microspheres	The formation of a hetero-junction can lower the recombination rate of the photo-excited electron-hole pairs and the small size of ZnO could improve light absorption properties.	[254]
Aerobic oxidation of alcohols	ZnO	Nanorods	The efficient separation of photo-generated charge carriers and its favorable, selective absorption toward the reactant of alcohols rather than the product of aldehydes, induced by the special 1D morphology of ZnO nanorods.	[261]
Reduction of Cr (VI)	GO-ZnO (doping)	Prismatic rod, Hexagonal tube-like	The oxygenated functional groups and the unique structures of 2D GO played pivotal roles in tuning the morphology of ZnO and increasing oxygen vacancies concentration. The introduction of oxygen vacancies and the intimate interfacial interaction between ZnO and reduced grapheneoxide (RGO) extended the light absorption edge of RGO-ZnO to the visible light region.	[262]

(1) Small particle size effects. A small particle size always means high surface area which can provide more active sites to facilitate mass transportation of the reactants and extend light absorption edge. In addition, it will accelerate the diffusion of the photo-induced electrons or holes from bulk to surface and suppress the recombination of the photo-generated electron-hole pairs. Furthermore, if the diameter of the nanowire is smaller than its critical value, the effective band gap of ZnO increases, as the redox potentials; therefore, the photo-generated charge carriers will demonstrate a higher reducing/oxidizing capability.

(2) High specific surface area effects. Besides more active sites, fast mass transportation of the reactants and extend light absorption edge, high specific surface area also promote the formation of defects.

(3) Defects (oxygen vacancies). It is commonly accepted that oxygen vacancies are electron trap sites which could therefore enhance the hole transfer reactions. Oxygen vacancies not only act as the active centers to influence the adsorption of reactants and the product selectivity, but also narrow the band gap of ZnO, deter photo-corrosion, decrease the recombination of electron-hole pairs, improving the catalytic activity.

(4) Polar facets. The terminal polar (001) and $(00\bar{1})$ facets have been proved to be more active for photo-catalysis than the non-polar facets, favorable for the adsorption of oxygen molecules and OH^- ions, resulting in higher generation rate of H_2O_2 and OH· radicals. Besides, the polar facets facilitate the production of oxygen vacancies.

(5) Orientation of ZnO arrays. The highly orientated ZnO arrays could also increase the polar facet exposing probabilities, leading to enhanced photo-catalytic properties.

(6) The hetero-junction and the special hierarchical architectures. These engineered structures could promote the separation and transportation of photo-excited electron-hole pairs and inhibit their recombination, enhancing photo-catalytic property.

(7) Morphology-dependent charge transfer effects. Two-electron transfer initiated reactions or multi-electron transfer reactions can be tuned by the number of defects, through the selection of optimal ZnO morphologies.

(8) Modification by sensitization through coupling with a narrow band gap semiconductor, forming nanocomposite photocatalyst and metal loading. All of these modifications are created to extend the light absorption to visible-light range. In addition, metal loading such as Ag and Au may cause SPR effects to further increase the photocatalytic properties.

(9) Modification by metal and non-metal doping. Metal doping decreases crystal particle size, increasing specific surface area and favoring the formation of defects. Furthermore, metal doping on one hand narrows the band gap by creating mid-gap level states, extending light absorption to the visible-light range; on the other hand these new states can act as charge recombination centers to deteriorate photocatalytic activity. Accordingly, nonmetal doping also favors formation of defects and narrows the band gap by elevating the valence band maximum to create a new valence band; thus, unlike metal doping, nonmetal doping is less likely to form recombination centers.

4. Application to Photo-Assisted Electro-Catalysis

Since oxide semiconductors were discovered employed as photoanodes in photoelectrochemical (PEC) cells to split water, it has become an exciting subject of research, as mentioned in the Introduction section [82–84,263]. However, in fact, photoelectron-oxidation of organic substances to produce hydrogen is much more efficient than PEC cells to split water [82]. Besides, photoelectron-oxidation of organic substances is also possible to produce electricity, called Photo Fuel Cell (PFC) [82]. The incorporation of large band-gap semiconductor photocatalysts is reported to efficiently minimize CO positioning in photoelectron oxidation of organic substances [83,84].

In the photoelectron oxidation of organic substances, ethanol and methanol fuel cells have attracted great attention. Leelavathi et al. demonstrated that amine-modified ZnO nanorods (passivated with oleylamine in their research) coated with ultra-thin Au (ZnO/Au) nanowires was

a promising catalyst for ethanol photoelectron oxidation [83]. The ZnO/Au nanowires exhibited an apparent enhancement in optical absorption, compared with ZnO/Au nanoparticles. It was found that ZnO nanorods passivated with oleylamine significantly increased its UV emission band edge (by ~1.5 times) which means there are electronic interactions between amine and ZnO. In addition, the degree of passivation increased along with the ratio of the concentration of oleylamine to ZnO; this further confirmed that amine interacted strongly with the ZnO surface. These strong electronic interactions played significant roles in photo-induced charge separation/recombination and Au nucleation. First, it accounted for the best possible separation of photo-generatedcharge carriers and also affected non-radiative recombination. Second, it preserved the electronic defect states that were responsible for the suppression of the charge carriers' recombination. In addition to these electronic effects, this interactions presented strong anchoring sites for the nucleation of Au nanoparticles that subsequently assisted in the growth of ultra thin Au wires. Besides, the geometric effects were also proposed to contribute a lot to the superior activity of ZnO/Au nanowires. Here, one-dimensional single crystalline nano-structures inherently possessed fewer defects as compared to nanoparticles, which led to the suppression of the recombination of charge carriers. Generally, defect sites are irreversibly oxidized under an applied potential which degrades the electro-catalytic performance. Second, the diffusion of electro-chemical species toward catalyst surfaces was significantly improved in high aspect ratio nanowires. Thirdly, inter-connected wires could also facilitate charge transport, thus enhancing electro-catalytic activity. Thus, the high photo-electro-catalytic activity of the ZnO/Au nanowire hybrid was ascribed to both electronic as well as geometric effects.

Similarly, Su et al. explored the electro-chemical performance of methanol oxidation over Pt@ZnO nano-rods @CC (CC: carbon cloth) electrode with or without UV irradiation [84]. With irradiation, Pt@ZnO@CC electrode demonstrated 90% higher methanol oxidation activity compared with commercial E-Tek, with the same loading of Pt. The results indicated that hydroxide species enriched on the ZnO nanorods' surface, facilitated CO removal through a bi-functional mechanism. Moreover, XPS characterization confirmed the charge transfer between Pt nanoparticles and ZnO nanorods, tuning the electronic structure of surface Pt, decreasing CO adsorption energy, and improving the electro-catalytic activity of methanol oxidation. When the catalyst surface was under the presence of UV irradiation, the chrono-amperometric response was increased about 62%. This increase was mainly due to the synergistic effects between the photo-oxidation of methanol on ZnO and the electro-oxidation of methanol on Pt. This synergistic effect originated from the high surface area and strong light absorption by ZnO nanorod arrays in the UV region.

5. Conclusions and Outlook

In summary, ZnO has been widely applied to green energy and environmental issues involving catalytic reactions, such as the industrial methanol synthesis, methanol steam reforming, hydro-desulfurization, photo-catalysis, photoelectro-catalysis etc.; and ZnO also exhibited apparent morphology-dependent catalytic performance in these reactions. As a significant semiconductor and catalytic material, ZnO has various energy-level configurations, surface atom distributions, surface energy, defects, acidity and basicity, and SMSI effects which greatly depend on its size, structure, morphology, and modification. Thus, similar to thermo-catalysis, particle size/specific surface area, the surface polarity of ZnO (surface energy, defects, acidity and basicity, and SMSI effects) tuned by ZnO morphologies are essential for photocatalytic and photoelectrocatalytic performance. Besides these factors, other morphology related factors such as orientation of ZnO arrays, special hierarchical architectures, engineered hetero-junctions and the surface polarity-dependent charge transfer effects are all critical in enhancing their photocatalytic and photoelectrocatalytic performance through increasing visible light harvesting, promoting the separation and transportation of the photo-excited charge carriers, and suppressing their recombination. In addition, other parameters rather than morphology-dependent ones, such as ZnO modification by sensitization through coupling with a narrow band gap semiconductor, forming nanocomposite photocatalysts, and metal loading are also

reported to narrow its band gap, extend light absorption to the visible-light range, and display SPR effects by loading Ag and Au, etc. In addition, ZnO modification by metal and nonmetal doping is widely considered to extend the absorption wavelength range, increase crystal defects, and/or increase specific surface area, and create charge carrier trap sites by modifying the electronic band structure of ZnO, then altering the photocatalytic and photoelectrocatalytic performance.

ZnO basted catalysis has attracted much attention and presents a rising interest as displayed above and surveyed by Samadi et al. [81]. As reviewed in Sections 2–4, morphology control strategy is a good approach to modify the catalytic activity of ZnO nanostructures for many reactions in both environmental and energy fields. However, the developement of catalytic applications of morphology controlled ZnO nanostructures have still a number of important issues concerning them, including the following:

i. Although there is abundant published work on doped ZnO nanostructures [80,81,258], large scale synthesis methods of doped ZnO particularly nonmetal doped ZnO with reguar morphologies should be further developed, which will enable its wide applications in catalysis.
ii. High specific surface area is beneficial for catalytic performance and some ZnO morphologies with meporous structures have been reported in the applications of catalysis [142,207,240,249]. However, this is a challenge because the morphology controlled synthesis may be destroyed by pore-forming materials and more research should be carried out.
iii. One-dimensional ZnO nanostructures have been intensively investigated in photoelectrochemical (PEC) cells to split water and large enhancements have been achieved [74,77,79,82–84]. Furthermore, ZnO nanorods have been reported in the applications of photoelectron-oxidation of ethanol and methanol [83,84]; ZnO has also been applied as an important photoelectrocatalyst component in the methanol production from CO_2 by photoelectrocatalytic reduction. Therefore, applications of morphology controlled ZnO in the photoelectron oxidation of organic substances to generate hydrogen or electricity and photoelectron reduction of CO_2 to produce fuels should be further investigated.
iv. ZnO based proper hierarchical architectures and hetero-junctions have been proven to be favorable for enhancing thermocatalytic properties [264]. Morphology controlled ZnO with special hierarchical architectures and hetero-junctions should be well developed and utilized in all kinds of thermocatalytic reactions. Similarly, metal and nonmetal doping can modify the electronic structures of ZnO; however, there is a lack of research on the thermocatalytic reactions of morphology controlled ZnO with doping. The development of these types of ZnO nanostructures on one hand will contribute to the improvement of catalytic performance; on the other hand, can be served as model catalyst to investigate complicated catalytic theories.

Acknowledgments: This work was financially supported by the National Natural Science Foundation of China (No. 21207039, 51108187, U1201231, B5151050), the Fundamental Research Funds for the Central Universities (No. 2015zz052, D215086w, D2154140), Guangzhou science and technology plan (201607010095) and the Natural Science Foundation of Guangdong Province, China (Grant No. S2011010000737).

Conflicts of Interest: The authors declare no conflict of interest.

References

1. Kołodziejczak-Radzimska, A.; Jesionowski, T. Zinc oxide-from synthesis to application: A review. *Materials* **2014**, *7*, 2833–2881. [CrossRef]
2. Segets, D.; Gradl, J.; Taylor, R.K.; Vassilev, V.; Peukert, W. Analysis of optical absorbance spectra for the determination of ZnO nanoparticle size distribution, solubility, and surface energy. *ACS Nano* **2009**, *3*, 1703–1710. [CrossRef] [PubMed]
3. Bacaksiz, E.; Parlak, M.; Tomakin, M.; Özçelik, A.; Karakız, M.; Altunbaş, M. The effects of zinc nitrate, zinc acetate and zinc chloride precursors on investigation of structural and optical properties of ZnO thin films. *J. Alloys Compd.* **2008**, *466*, 447–450. [CrossRef]

4. Wang, J.; Cao, J.; Fang, B.; Lu, P.; Deng, S.; Wang, H. Synthesis and characterization of multipod, flower-like, and shuttle-like ZnO frameworks in ionic liquids. *Mater. Lett.* **2005**, *59*, 1405–1408. [CrossRef]
5. Wang, Z.L. Splendid one-dimensional nanostructures of zinc oxide: A new nanomaterial family for nanotechnology. *ACS Nano* **2008**, *2*, 1987–1992. [CrossRef] [PubMed]
6. Chaari, M.; Matoussi, A. Electrical conduction and dielectric studies of ZnO pellets. *Phys. B Condens. Matter* **2012**, *407*, 3441–3447. [CrossRef]
7. Cheng, S.; Yan, D.; Chen, J.; Zhuo, R.; Feng, J.; Li, H.; Feng, H.; Yan, P. Soft-template synthesis and characterization of ZnO and ZnO hollow spheres. *J. Phys. Chem. C* **2009**, *113*, 13630–13635. [CrossRef]
8. Chen, Y.; Zhao, H.; Liu, B.; Yang, H. Charge separation between wurtzite ZnO polar {001} surfaces and their enhanced photocatalytic activity. *Appl. Catal. B* **2015**, *163*, 189–197. [CrossRef]
9. Grätzel, M. Photoelectrochemical cells. *Nature* **2001**, *414*, 338–344. [CrossRef] [PubMed]
10. Liao, F.; Huang, Y.; Ge, J.; Zheng, W.; Tedsree, K.; Collier, P.; Hong, X.; Tsang, S.C. Morphology-dependent interactions of ZnO with Cu nanoparticles at the materials' interface in selective hydrogenation of CO_2 to CH_3OH. *Angew. Chem. Int. Ed.* **2011**, *50*, 2162–2165. [CrossRef] [PubMed]
11. Hu, J.; Fan, Y.; Pei, Y.; Qiao, M.; Fan, K.; Zhang, X.; Zong, B. Shape effect of ZnO crystals as cocatalyst in combined reforming–hydrogenolysis of glycerol. *ACS Catal.* **2013**, *3*, 2280–2287. [CrossRef]
12. Schumann, J.; Eichelbaum, M.; Lunkenbein, T.; Thomas, N.; Alvarez Galvan, M.C.; Schlogl, R.; Behrens, M. Promoting strong metal support interaction: Doping ZnO for enhanced activity of Cu/ZnO:M (M = Al, Ga, Mg) catalysts. *ACS Catal.* **2015**, *5*, 3260–3270. [CrossRef]
13. Zhang, H.; Sun, J.; Dagle, V.L.; Halevi, B.; Datye, A.K.; Wang, Y. Influence of ZnO facets on Pd/ZnO catalysts for methanol steam reforming. *ACS Catal.* **2014**, *4*, 2379–2386. [CrossRef]
14. Xu, L.; Hu, Y.-L.; Pelligra, C.; Chen, C.-H.; Jin, L.; Huang, H.; Sithambaram, S.; Aindow, M.; Joesten, R.; Suib, S.L. ZnO with different morphologies synthesized by solvothermal methods for enhanced photocatalytic activity. *Chem. Mater.* **2009**, *21*, 2875–2885. [CrossRef]
15. Kuld, S.; Thorhauge, M.; Falsig, H.; Elkjær, C.F.; Helveg, S.; Chorkendorff, I.; Sehested, J. Quantifying the promotion of Cu catalysts by ZnO for methanol synthesis. *Science* **2016**, *352*, 969–974. [CrossRef] [PubMed]
16. Ernst, K.; Ludviksson, A.; Zhang, R.; Yoshihara, J.; Campbell, C. Growth model for metal films on oxide surfaces: Cu on ZnO(000–1). *Phys. Rev. B* **1993**, *47*, 13782. [CrossRef]
17. Jacek, G.; Fabio, F.; Claudine, N. Polarity of oxide surfaces and nanostructures. *Rep. Prog. Phys.* **2008**, *71*, 016501.
18. Schimpf, S.; Rittermeier, A.; Zhang, X.; Li, Z.A.; Spasova, M.; van den Berg, M.W.; Farle, M.; Wang, Y.; Fischer, R.A.; Muhler, M. Stearate-based Cu colloids in methanol synthesis: Structural changes driven by strong metal–support interactions. *ChemCatChem* **2010**, *2*, 214–222. [CrossRef]
19. Sirbuly, D.J.; Law, M.; Yan, H.; Yang, P. Semiconductor nanowires for subwavelength photonics integration. *J. Phys. Chem. B* **2005**, *109*, 15190–15213. [CrossRef] [PubMed]
20. Wang, Z.; Wang, F.; Lu, Y.; Xu, M.; Li, Q. Induction of zinc particles on the morphology and photoluminescent property of globular Zn/ZnO core/shell nanorod heterojunction array architectures. *J. Exp. Nanosci.* **2015**, *11*, 1–12. [CrossRef]
21. Heo, Y.; Tien, L.; Norton, D.; Pearton, S.; Kang, B.; Ren, F.; LaRoche, J. Pt/ZnO nanowire schottky diodes. *Appl. Phys. Lett.* **2004**, *85*, 3107–3109. [CrossRef]
22. Barth, S.; Hernandez-Ramirez, F.; Holmes, J.D.; Romano-Rodriguez, A. Synthesis and applications of one-dimensional semiconductors. *Prog. Mater. Sci.* **2010**, *55*, 563–627. [CrossRef]
23. Devan, R.S.; Patil, R.A.; Lin, J.H.; Ma, Y.R. One-dimensional metal-oxide nanostructures: Recent developments in synthesis, characterization, and applications. *Adv. Funct. Mater.* **2012**, *22*, 3326–3370. [CrossRef]
24. Xu, S.; Wang, Z.L. One-dimensional ZnO nanostructures: Solution growth and functional properties. *Nano Res.* **2011**, *4*, 1013–1098. [CrossRef]
25. Wu, J.-J.; Liu, S.-C. Low-temperature growth of well-aligned ZnO nanorods by chemical vapor deposition. *Adv. Mater.* **2002**, *14*, 215–218. [CrossRef]
26. Kahn, M.L.; Monge, M.; Snoeck, E.; Maisonnat, A.; Chaudret, B. Spontaneous formation of ordered 2D and 3D superlattices of ZnO nanocrystals. *Small* **2005**, *1*, 221–224. [CrossRef] [PubMed]
27. Alenezi, M.R.; Henley, S.J.; Emerson, N.G.; Silva, S.R.P. From 1d and 2D ZnO nanostructures to 3D hierarchical structures with enhanced gas sensing properties. *Nanoscale* **2014**, *6*, 235–247. [CrossRef] [PubMed]

28. Wang, X.; Liu, W.; Liu, J.; Wang, F.; Kong, J.; Qiu, S.; He, C.; Luan, L. Synthesis of nestlike ZnO hierarchically porous structures and analysis of their gas sensing properties. *ACS Appl. Mater. Int.* **2012**, *4*, 817–825. [CrossRef] [PubMed]
29. Joshi, R.K.; Schneider, J.J. Assembly of one dimensional inorganic nanostructures into functional 2D and 3D architectures. Synthesis, arrangement and functionality. *Chem. Soc. Rev.* **2012**, *41*, 5285–5312. [CrossRef] [PubMed]
30. Li, Y.; Cai, W.; Duan, G.; Cao, B.; Sun, F.; Lu, F. Superhydrophobicity of 2D ZnO ordered pore arrays formed by solution-dipping template method. *J. Colloid Interface Sci.* **2005**, *287*, 634–639. [CrossRef] [PubMed]
31. Lu, W.; Gao, S.; Wang, J. One-pot synthesis of Ag/ZnO self-assembled 3D hollow microspheres with enhanced photocatalytic performance. *J. Phys. Chem. C* **2008**, *112*, 16792–16800. [CrossRef]
32. Vayssieres, L.; Keis, K.; Lindquist, S.-E.; Hagfeldt, A. Purpose-built anisotropic metal oxide material: 3D highly oriented microrod array of ZnO. *J. Phys. Chem. B* **2001**, *105*, 3350–3352. [CrossRef]
33. Banerjee, D.; Lao, J.; Wang, D.; Huang, J.; Ren, Z.; Steeves, D.; Kimball, B.; Sennett, M. Large-quantity free-standing ZnO nanowires. *Appl. Phys. Lett.* **2003**, *83*, 2061–2063. [CrossRef]
34. Hahn, Y.-B. Zinc oxide nanostructures and their applications. *Korean J. Chem. Eng.* **2011**, *28*, 1797–1813. [CrossRef]
35. Frade, T.; Jorge, M.M.; Gomes, A. One-dimensional ZnO nanostructured films: Effect of oxide nanoparticles. *Mater. Lett.* **2012**, *82*, 13–15. [CrossRef]
36. Wu, J.-J.; Liu, S.-C.; Wu, C.-T.; Chen, K.-H.; Chen, L.-C. Heterostructures of ZnO-Zn coaxial nanocables and ZnO nanotubes. *Appl. Phys. Lett.* **2002**, *81*, 1312–1314. [CrossRef]
37. Chen, W.; Liu, W.; Hsieh, S.; Tsai, T. Preparation of nanosized ZnO using α brass. *Appl. Surf. Sci.* **2007**, *253*, 6749–6753. [CrossRef]
38. Liu, J.; Huang, X.; Duan, J.; Ai, H.; Tu, P. A low-temperature synthesis of multi whisker-based zinc oxide micron crystals. *Mater. Lett.* **2005**, *59*, 3710–3714. [CrossRef]
39. Huang, Y.; He, J.; Zhang, Y.; Dai, Y.; Gu, Y.; Wang, S.; Zhou, C. Morphology, structures and properties of ZnO nanobelts fabricated by Zn-powder evaporation without catalyst at lower temperature. *J. Mater. Sci.* **2006**, *41*, 3057–3062. [CrossRef]
40. Nikoobakht, B.; Wang, X.; Herzing, A.; Shi, J. Scalable synthesis and device integration of self-registered one-dimensional zinc oxide nanostructures and related materials. *Chem. Soc. Rev.* **2013**, *42*, 342–365. [CrossRef] [PubMed]
41. Tien, L.; Pearton, S.; Norton, D.; Ren, F. Synthesis and microstructure of vertically aligned ZnO nanowires grown by high-pressure-assisted pulsed-laser deposition. *J. Mater. Sci.* **2008**, *43*, 6925–6932. [CrossRef]
42. Cui, J. Zinc oxide nanowires. *Mater. Charact.* **2012**, *64*, 43–52. [CrossRef]
43. Wahab, R.; Ansari, S.; Kim, Y.-S.; Seo, H.-K.; Shin, H.-S. Room temperature synthesis of needle-shaped ZnO nanorods via sonochemical method. *Appl. Surf. Sci.* **2007**, *253*, 7622–7626. [CrossRef]
44. Hughes, W.L.; Wang, Z.L. Formation of piezoelectric single-crystal nanorings and nanobows. *J. Am. Chem. Soc.* **2004**, *126*, 6703–6709. [CrossRef] [PubMed]
45. Xu, T.; Ji, P.; He, M.; Li, J. Growth and structure of pure ZnO micro/nanocombs. *J. Nanomater.* **2012**, *2012*, 1–5. [CrossRef]
46. Kong, X.Y.; Wang, Z.L. Spontaneous polarization-induced nanohelixes, nanosprings, and nanorings of piezoelectric nanobelts. *Nano Lett.* **2003**, *3*, 1625–1631. [CrossRef]
47. Snure, M.; Tiwari, A. Synthesis, characterization, and green luminescence in ZnO nanocages. *J. Nanosci. Nanotechnol.* **2007**, *7*, 481–485. [CrossRef]
48. Chiu, W.; Khiew, P.; Cloke, M.; Isa, D.; Tan, T.; Radiman, S.; Abd-Shukor, R.; Hamid, M.A.; Huang, N.; Lim, H. Photocatalytic study of two-dimensional ZnO nanopellets in the decomposition of methylene blue. *Chem. Eng. J.* **2010**, *158*, 345–352. [CrossRef]
49. Jose-Yacaman, M.; Gutierrez-Wing, C.; Miki, M.; Yang, D.-Q.; Piyakis, K.; Sacher, E. Surface diffusion and coalescence of mobile metal nanoparticles. *J. Phys. Chem. B* **2005**, *109*, 9703–9711. [CrossRef] [PubMed]
50. Polshettiwar, V.; Baruwati, B.; Varma, R.S. Self-assembly of metal oxides into three-dimensional nanostructures: Synthesis and application in catalysis. *ACS Nano* **2009**, *3*, 728–736. [CrossRef] [PubMed]
51. Xie, Q.; Dai, Z.; Liang, J.; Xu, L.; Yu, W.; Qian, Y. Synthesis of ZnO three-dimensional architectures and their optical properties. *Solid State Commun.* **2005**, *136*, 304–307. [CrossRef]

52. Liu, J.; Huang, X.; Li, Y.; Sulieman, K.; Sun, F.; He, X. Selective growth and properties of zinc oxide nanostructures. *Scr. Mater.* **2006**, *55*, 795–798. [CrossRef]
53. Bitenc, M.; Orel, Z.C. Synthesis and characterization of crystalline hexagonal bipods of zinc oxide. *Mater. Res. Bull.* **2009**, *44*, 381–387. [CrossRef]
54. Fan, Z.; Lu, J.G. Zinc oxide nanostructures: Synthesis and properties. *J. Nanosci. Nanotechnol.* **2005**, *5*, 1561–1573. [CrossRef] [PubMed]
55. Yi, G.-C.; Wang, C.; Park, W.I. ZnO nanorods: Synthesis, characterization and applications. *Semicond. Sci. Technol.* **2005**, *20*, S22–S34. [CrossRef]
56. Heo, Y.W.; Norton, D.; Tien, L.; Kwon, Y.; Kang, B.; Ren, F.; Pearton, S.; LaRoche, J. ZnO nanowire growth and devices. *Mater. Sci. Eng. A-Struct. R: Rep.* **2004**, *47*, 1–47. [CrossRef]
57. Özgür, Ü.; Alivov, Y.I.; Liu, C.; Teke, A.; Reshchikov, M.; Doğan, S.; Avrutin, V.; Cho, S.-J.; Morkoc, H. A comprehensive review of ZnO materials and devices. *J. Appl. Phys.* **2005**, *98*, 041301. [CrossRef]
58. Klingshirn, C. ZnO: From basics towards applications. *Phys. Status Solidi B* **2007**, *244*, 3027–3073. [CrossRef]
59. Klingshirn, C. ZnO: Material, physics and applications. *Chem. Phys. Chem.* **2007**, *8*, 782–803. [CrossRef] [PubMed]
60. Djurišić, A.B.; Leung, Y.H. Optical properties of ZnO nanostructures. *Small* **2006**, *2*, 944–961. [CrossRef] [PubMed]
61. Janotti, A.; Van de Walle, C.G. Fundamentals of zinc oxide as a semiconductor. *Rep. Prog. Phys.* **2009**, *72*, 126501. [CrossRef]
62. Baruah, S.; Dutta, J. Hydrothermal growth of ZnO nanostructures. *Sci. Technol. Adv. Mater.* **2009**, *1*, 013001. [CrossRef] [PubMed]
63. Ellmer, K.; Klein, A.; Rech, B. *Transparent Conductive Zinc Oxide: Basics and Applications in Thin Film Solar Cells*; Springer Science & Business Media: Berlin, Germany, 2007.
64. Wöll, C. The chemistry and physics of zinc oxide surfaces. *Prog. Surf. Sci.* **2007**, *82*, 55–120. [CrossRef]
65. McCluskey, M.; Jokela, S. Defects in ZnO. *J. Appl. Phys.* **2009**, *106*, 071101. [CrossRef]
66. Djurišić, A.; Ng, A.; Chen, X. ZnO nanostructures for optoelectronics: Material properties and device applications. *Prog. Quant. Electron.* **2010**, *34*, 191–259. [CrossRef]
67. Djurišić, A.B.; Chen, X.; Leung, Y.H.; Ng, A.M.C. ZnO nanostructures: Growth, properties and applications. *J. Mater. Chem.* **2012**, *22*, 6526–6535. [CrossRef]
68. Djurišić, A.B.; Liu, X.; Leung, Y.H. Zinc oxide films and nanomaterials for photovoltaic applications. *Phys. Status Solidi-R* **2014**, *8*, 123–132. [CrossRef]
69. Feng, K.; Li, W.; Xie, S.; Lu, X. Nickel hydroxide decorated hydrogenated zinc oxide nanorod arrays with enhanced photoelectrochemical performance. *Electrochim. Acta* **2014**, *137*, 108–113. [CrossRef]
70. Kozuka, Y.; Tsukazaki, A.; Kawasaki, M. Challenges and opportunities of ZnO-related single crystalline heterostructures. *Appl. Phys. Rev.* **2014**, *1*, 011303. [CrossRef]
71. Kumar, R.; Kumar, G.; Al-Dossary, O.; Umar, A. ZnO nanostructured thin films: Depositions, properties and applications-a review. *Mater. Express* **2015**, *5*, 3–23. [CrossRef]
72. Sengupta, D.; Das, P.; Mondal, B.; Mukherjee, K. Effects of doping, morphology and film-thickness of photo-anode materials for dye sensitized solar cell application-a review. *Renew. Sustain. Energy Rev.* **2016**, *60*, 356–376. [CrossRef]
73. Moezzi, A.; McDonagh, A.M.; Cortie, M.B. Zinc oxide particles: Synthesis, properties and applications. *Chem. Eng. J.* **2012**, *185*, 1–22. [CrossRef]
74. Johar, M.A.; Afzal, R.A.; Alazba, A.A.; Manzoor, U. Photocatalysis and Band gap Engineering Using ZnO Nanocomposites. *Adv. Mater. Sci. Eng.* **2015**, *2015*, 934587.
75. Lee, K.M.; Lai, C.W.; Ngai, K.S.; Juan, J.C. Recent developments of zinc oxide based photocatalyst in water treatment technology: A review. *Water. Res.* **2016**, *88*, 428–448. [CrossRef] [PubMed]
76. KSR, K.K.R. Zinc oxide based photocatalysis: Tailoring surface-bulk structure and related interfacial charge carrier dynamics for better environmental applications. *RSC Adv.* **2015**, *5*, 3306–3351.
77. Kulmas, M.; Paterson, L.; Höflich, K.; Bashouti, M.Y.; Wu, Y.; Göbelt, M.; Ristein, J.; Bachmann, J.; Meyer, B.; Christiansen, S. Composite nanostructures of TiO_2 and ZnO for water splitting application: Atomic layer deposition growth and density functional theory investigation. *Adv. Funct. Mater.* **2016**, *26*, 4882–4889. [CrossRef]

78. Sudha, D.; Sivakumar, P. Review on the photocatalytic activity of various composite catalysts. *Chem. Eng. Process.* **2015**, *97*, 112–133. [CrossRef]
79. Zhang, Y.; Ram, M.K.; Stefanakos, E.K.; Goswami, D.Y. Synthesis, characterization, and applications of ZnO nanowires. *J. Nanomater.* **2012**, *2012*, 1–22. [CrossRef]
80. Djerdj, I.; Jagličić, Z.; Arčon, D.; Niederberger, M. Co-doped ZnO nanoparticles: Minireview. *Nanoscale* **2010**, *2*, 1096–1104. [CrossRef] [PubMed]
81. Samadi, M.; Zirak, M.; Naseri, A.; Khorashadizade, E.; Moshfegh, A.Z. Recent progress on doped ZnO nanostructures for visible-light photocatalysis. *Thin Solid Films* **2016**, *605*, 2–19. [CrossRef]
82. Antoniadou, M.; Lianos, P. Production of electricity by photoelectrochemical oxidation. *Appl. Catal. B* **2010**, *99*, 307–313. [CrossRef]
83. Leelavathi, A.; Madras, G.; Ravishankar, N. New insights into electronic and geometric effects in the enhanced photoelectrooxidation of ethanol using ZnO nanorod/ultrathin au nanowire hybrids. *J. Am. Chem. Soc.* **2014**, *136*, 14445. [CrossRef] [PubMed]
84. Su, C.-Y.; Hsueh, Y.-C.; Kei, C.-C.; Lin, C.-T.; Perng, T.-P. Fabrication of high-activity hybrid Pt@ZnO catalyst on carbon cloth by atomic layer deposition for photoassisted electro-oxidation of methanol. *J. Phys. Chem. C* **2013**, *117*, 11610–11618. [CrossRef]
85. Hewlett, R.M.; McLachlan, M.A. Surface structure modification of ZnO and the impact on electronic properties. *Adv. Mater.* **2016**, *28*, 3893–3921. [CrossRef] [PubMed]
86. Ariffin, S.; Lim, H.; Talib, Z.; Pandikumar, A.; Huang, N. Aerosol-assisted chemical vapor deposition of metal oxide thin films for photoelectrochemical water splitting. *Int. J. Hydrog. Energy* **2015**, *40*, 2115–2131. [CrossRef]
87. Chen, H.M.; Chen, C.K.; Liu, R.-S.; Zhang, L.; Zhang, J.; Wilkinson, D.P. Nano-architecture and material designs for water splitting photoelectrodes. *Chem. Soc. Rev.* **2012**, *41*, 5654–5671. [CrossRef] [PubMed]
88. Xiao, F.X.; Miao, J.; Tao, H.B.; Hung, S.F.; Wang, H.Y.; Yang, H.B.; Chen, J.; Chen, R.; Liu, B. One-dimensional hybrid nanostructures for heterogeneous photocatalysis and photoelectrocatalysis. *Small* **2015**, *11*, 2115–2131. [CrossRef] [PubMed]
89. Rajaambal, S.; Sivaranjani, K.; Gopinath, C.S. Recent developments in solar H_2 generation from water splitting. *J. Chem. Sci.* **2015**, *127*, 33–47. [CrossRef]
90. Moniz, S.J.; Shevlin, S.A.; Martin, D.J.; Guo, Z.-X.; Tang, J. Visible-light driven heterojunction photocatalysts for water splitting—A critical review. *Energy Environ. Sci.* **2015**, *8*, 731–759. [CrossRef]
91. Maeda, K.; Domen, K. Solid solution of gan and ZnO as a stable photocatalyst for overall water splitting under visible light. *Chem. Mater.* **2010**, *22*, 612–623. [CrossRef]
92. Rao, C.N.R.; Lingampalli, S.R.; Dey, S.; Roy, A. Solar photochemical and thermochemical splitting of water. *Philos. Trans. R. Soc. A* **2016**, *374*, 20150088. [CrossRef] [PubMed]
93. Chen, X.; Zhang, Z.; Chi, L.; Nair, A.K.; Shangguan, W.; Jiang, Z. Recent advances in visible-light-driven photoelectrochemical water splitting: Catalyst nanostructures and reaction systems. *Nano-Micro Lett.* **2016**, *8*, 1–12. [CrossRef]
94. Mao, S.S.; Shen, S.; Guo, L. Nanomaterials for renewable hydrogen production, storage and utilization. *Prog. Nat. Sci. Mater.* **2012**, *22*, 522–534. [CrossRef]
95. Huang, C.-H.; Tan, C.-S. A review: CO_2 utilization. *Aerosol. Air Qual. Res.* **2014**, *14*, 480–499. [CrossRef]
96. Schüth, F. Chemical compounds for energy storage. *Chem. Ing. Tech.* **2011**, *83*, 1984–1993. [CrossRef]
97. Quadrelli, E.A.; Centi, G.; Duplan, J.L.; Perathoner, S. Carbon dioxide recycling: Emerging large-scale technologies with industrial potential. *ChemSusChem* **2011**, *4*, 1194–1215. [CrossRef] [PubMed]
98. Studt, F.; Behrens, M.; Kunkes, E.L.; Thomas, N.; Zander, S.; Tarasov, A.; Schumann, J.; Frei, E.; Varley, J.B.; Abild-Pedersen, F. The mechanism of CO and CO_2 hydrogenation to methanol over Cu-based catalysts. *ChemCatChem* **2015**, *7*, 1105–1111. [CrossRef]
99. Vesborg, P.C.; Chorkendorff, I.; Knudsen, I.; Balmes, O.; Nerlov, J.; Molenbroek, A.M.; Clausen, B.S.; Helveg, S. Transient behavior of Cu/ZnO-based methanol synthesis catalysts. *J. Catal.* **2009**, *262*, 65–72. [CrossRef]
100. Morkoç, H.; Özgür, Ü. *Zinc Oxide: Fundamentals, Materials and Device Technology*; John Wiley & Sons: Virginia, VA, USA, 2008.
101. Wang, H.; Lu, Z.; Lu, D.; Li, C.; Fang, P.; Wang, X. The synthesis of Cu/plate-like ZnO nanostructures and their self-assembly mechanism. *Solid State Sci.* **2016**, *55*, 69–76. [CrossRef]

102. Lei, H.; Nie, R.; Wu, G.; Hou, Z. Hydrogenation of CO_2 to CH_3OH over Cu/ZnO catalysts with different ZnO morphology. *Fuel* **2015**, *154*, 161–166. [CrossRef]
103. Güder, F.; Frei, E.; Kücükbayrak, U.M.; Menzel, A.; Thomann, R.; Luptak, R.; Hollaender, B.; Krossing, I.; Zacharias, M. Engineered high aspect ratio vertical nanotubes as a model system for the investigation of catalytic methanol synthesis over Cu/ZnO. *ACS Appl. Mater. Int.* **2014**, *6*, 1576–1582. [CrossRef] [PubMed]
104. Wei, Z.; Sun, J.; Li, Y.; Datye, A.K.; Wang, Y. Bimetallic catalysts for hydrogen generation. *Chem. Soc. Rev.* **2012**, *41*, 7994–8008. [CrossRef] [PubMed]
105. Davidson, S.D.; Zhang, H.; Sun, J.; Wang, Y. Supported metal catalysts for alcohol/sugar alcohol steam reforming. *Dalton Trans.* **2014**, *43*, 11782–11802. [CrossRef] [PubMed]
106. Sá, S.; Silva, H.; Brandão, L.; Sousa, J.M.; Mendes, A. Catalysts for methanol steam reforming—A review. *Appl. Catal. B* **2010**, *99*, 43–57. [CrossRef]
107. Holladay, J.D.; Wang, Y. A review of recent advances in numerical simulations of microscale fuel processor for hydrogen production. *J. Power Sources* **2015**, *282*, 602–621. [CrossRef]
108. Xia, G.; Holladay, J.D.; Dagle, R.A.; Jones, E.O.; Wang, Y. Development of highly active Pd-ZnO/Al_2O_3 catalysts for microscale fuel processor applications. *Chem. Eng. Technol.* **2005**, *28*, 515–519. [CrossRef]
109. Danwittayakul, S.; Dutta, J. Two step copper impregnated zinc oxide microball synthesis for the reduction of activation energy of methanol steam reformation. *Chem. Eng. J.* **2013**, *223*, 304–308. [CrossRef]
110. Matsumura, Y.; Ishibe, H. High temperature steam reforming of methanol over Cu/ZnO/ZrO_2 catalysts. *Appl. Catal. B* **2009**, *91*, 524–532. [CrossRef]
111. Matsumura, Y.; Ishibe, H. Suppression of CO by-production in steam reforming of methanol by addition of zinc oxide to silica-supported copper catalyst. *J. Catal.* **2009**, *268*, 282–289. [CrossRef]
112. Liu, S.; Takahashi, K.; Fuchigami, K.; Uematsu, K. Hydrogen production by oxidative methanol reforming on Pd/ZnO: Catalyst deactivation. *Appl. Catal. A* **2006**, *299*, 58–65. [CrossRef]
113. Lin, Y.-G.; Hsu, Y.-K.; Chen, S.-Y.; Lin, Y.-K.; Chen, L.-C.; Chen, K.-H. Nanostructured zinc oxide nanorods with copper nanoparticles as a microreformation catalyst. *Angew. Chem. Int. Ed.* **2009**, *48*, 7586–7590. [CrossRef] [PubMed]
114. Karim, A.M.; Conant, T.; Datye, A.K. Controlling ZnO morphology for improved methanol steam reforming reactivity. *Phys. Chem. Chem. Phys.* **2008**, *10*, 5584–5590. [CrossRef] [PubMed]
115. Karim, A.; Conant, T.; Datye, A. The role of PdZn alloy formation and particle size on the selectivity for steam reforming of methanol. *J. Catal.* **2006**, *243*, 420–427. [CrossRef]
116. Dagle, R.A.; Chin, Y.-H.; Wang, Y. The effects of PdZn crystallite size on methanol steam reforming. *Top. Catal.* **2007**, *46*, 358–362. [CrossRef]
117. Halevi, B.; Lin, S.; Roy, A.; Zhang, H.; Jeroro, E.; Vohs, J.; Wang, Y.; Guo, H.; Datye, A.K. High CO_2 selectivity of ZnO powder catalysts for methanol steam reforming. *J. Phys. Chem. C* **2013**, *117*, 6493–6503. [CrossRef]
118. Eblagon, K.M.; Concepción, P.H.; Silva, H.; Mendes, A. Ultraselective low temperature steam reforming of methanol over PdZn/ZnO catalysts—Influence of induced support defects on catalytic performance. *Appl. Catal. B* **2014**, *154–155*, 316–328. [CrossRef]
119. Maceiras, R.; Vega, M.; Costa, C.; Ramos, P.; Márquez, M. Effect of methanol content on enzymatic production of biodiesel from waste frying oil. *Fuel* **2009**, *88*, 2130–2134. [CrossRef]
120. Bhuiya, M.M.K.; Rasul, M.G.; Khan, M.M.K.; Ashwath, N.; Azad, A.K. Prospects of 2nd generation biodiesel as a sustainable fuel—Part 1: Selection of feedstocks, oil extraction techniques and conversion technologies. *Renew. Sustain. Energy Rev.* **2016**, *55*, 1109–1128. [CrossRef]
121. Bhuiya, M.M.K.; Rasul, M.G.; Khan, M.M.K.; Ashwath, N.; Azad, A.K.; Hazrat, M.A. Prospects of 2nd generation biodiesel as a sustainable fuel—Part 2: Properties, performance and emission characteristics. *Renew. Sustain. Energy Rev.* **2016**, *55*, 1129–1146. [CrossRef]
122. Takisawa, K.; Kanemoto, K.; Kartikawati, M.; Kitamura, Y. Simultaneous hydrolysis-esterification of wet microalgal lipid using acid. *Bioresour. Technol.* **2013**, *149*, 16–21. [CrossRef] [PubMed]
123. Song, C.; Liu, Q.; Ji, N.; Deng, S.; Zhao, J.; Li, S.; Kitamura, Y. Evaluation of hydrolysis–esterification biodiesel production from wet microalgae. *Bioresour. Technol.* **2016**, *214*, 747–754. [CrossRef] [PubMed]
124. Liu, F.; Zhang, Y. Controllable growth of "multi-level tower" ZnO for biodiesel production. *Ceram. Int.* **2011**, *37*, 3193–3202. [CrossRef]
125. Di Cosimo, J.; Dıez, V.; Xu, M.; Iglesia, E.; Apesteguıa, C. Structure and surface and catalytic properties of Mg-Al basic oxides. *J. Catal.* **1998**, *178*, 499–510. [CrossRef]

126. Van Santen, R.A.; Neurock, M. *Molecular Heterogeneous Catalysis: A Conceptual and Computational Approach*; John Wiley & Sons: Eindhoved, The Netherlands, 2009.
127. Chorkendorff, I.; Niemantsverdriet, J.W. *Concepts of Modern Catalysis and Kinetics*; John Wiley & Sons: Lyngby, Denmark, 2006.
128. Yan, S.; Salley, S.O.; Ng, K.S. Simultaneous transesterification and esterification of unrefined or waste oils over ZnO-La_2O_3 catalysts. *Appl. Catal. A* **2009**, *353*, 203–212. [CrossRef]
129. Zhang, H.; Sun, J.; Liu, C.; Wang, Y. Distinct water activation on polar/non-polar facets of ZnO nanoparticles. *J. Catal.* **2015**, *331*, 57–62. [CrossRef]
130. Morales, M.V.; Asedegbega-Nieto, E.; Iglesias-Juez, A.; Rodríguez-Ramos, I.; Guerrero-Ruiz, A. Role of exposed surfaces on zinc oxide nanostructures in the catalytic ethanol transformation. *ChemSusChem* **2015**, *8*, 2223–2230. [CrossRef] [PubMed]
131. Zhou, Y.; Lawrence, N.J.; Wu, T.S.; Liu, J.; Kent, P.; Soo, Y.L.; Cheung, C.L. Pd/CeO_2-*x* nanorod catalysts for CO oxidation: Insights into the origin of their regenerative ability at room temperature. *ChemCatChem* **2014**, *6*, 2937–2946. [CrossRef]
132. Liu, B.; Liu, J.; Li, T.; Zhao, Z.; Gong, X.-Q.; Chen, Y.; Duan, A.; Jiang, G.; Wei, Y. Interfacial effects of CeO_2-supported Pd nanorod in catalytic CO oxidation: A theoretical study. *J. Phys. Chem. C* **2015**, *119*, 12923–12934. [CrossRef]
133. Chen, G.; Xu, Q.; Yang, Y.; Li, C.; Huang, T.; Sun, G.; Zhang, S.; Ma, D.; Li, X. Facile and mild strategy to construct mesoporous CeO_2-CuO nanorods with enhanced catalytic activity toward co oxidation. *ACS Appl. Mater. Interfaces* **2015**, *7*, 23538–23544. [CrossRef] [PubMed]
134. Zhang, P.; Yu, H.; Li, J.; Zhao, H.; Zhu, B.; Huang, W.; Zhang, S. Au/$BiPO_4$ nanorod catalysts: Synthesis, characterization and their catalytic performance for CO oxidation. *RSC Adv.* **2016**, *6*, 15304–15312. [CrossRef]
135. Liu, B.; Zhao, Z.; Henkelman, G.; Song, W. Computational design of a CeO_2-supported Pd-based bimetallic nanorod for CO oxidation. *J. Phys. Chem. C* **2016**, *120*, 5557–5564. [CrossRef]
136. Chen, S.-Y.; Song, W.; Lin, H.-J.; Wang, S.; Biswas, S.; Mollahosseini, M.; Kuo, C.-H.; Gao, P.-X.; Suib, S.L. Manganese oxide nano-array based monolithic catalysts: Tunable morphology and high efficiency for CO oxidation. *ACS Appl. Mater. Interfaces* **2016**, *8*, 7834–7842. [CrossRef] [PubMed]
137. Liu, J.; Qiao, B.; Song, Y.; Huang, Y.; Liu, J.J. Hetero-epitaxially anchoring Au nanoparticles onto ZnO nanowires for CO oxidation. *Chem. Commun.* **2015**, *51*, 15332–15335. [CrossRef] [PubMed]
138. Liu, J.; Qiao, B.; Song, Y.; Tang, H.; Huang, Y.; Liu, J. Highly active and sintering-resistant heteroepitaxy of Au nanoparticles on ZnO nanowires for CO oxidation. *J. Energy Chem.* **2016**, *25*, 361–370. [CrossRef]
139. Liu, X.; Liu, M.-H.; Luo, Y.-C.; Mou, C.-Y.; Lin, S.D.; Cheng, H.; Chen, J.-M.; Lee, J.-F.; Lin, T.-S. Strong metal-support interactions between gold nanoparticles and ZnO nanorods in CO oxidation. *J. Am. Chem. Soc.* **2012**, *134*, 10251–10258. [CrossRef] [PubMed]
140. Carabineiro, S.; Machado, B.; Bacsa, R.; Serp, P.; Dražić, G.; Faria, J.; Figueiredo, J. Catalytic performance of Au/ZnO nanocatalysts for CO oxidation. *J. Catal.* **2010**, *273*, 191–198. [CrossRef]
141. Liu, M.-H.; Chen, Y.-W.; Liu, X.; Kuo, J.-L.; Chu, M.-W.; Mou, C.-Y. Defect-mediated gold substitution doping in ZnO mesocrystals and catalysis in CO oxidation. *ACS Catal.* **2015**, *6*, 115–122. [CrossRef]
142. Peng, S.-Y.; Xu, Z.-N.; Chen, Q.-S.; Wang, Z.-Q.; Lv, D.-M.; Sun, J.; Chen, Y.; Guo, G.-C. Enhanced stability of Pd/ZnO catalyst for CO oxidative coupling to dimethyl oxalate: Effect of Mg^{2+} doping. *ACS Catal.* **2015**, *5*, 4410–4417. [CrossRef]
143. Ali, S.A.; Ahmed, S.; Ahmed, K.W.; Al-Saleh, M.A. Simultaneous hydrodesulfurization of dibenzothiophene and substituted dibenzothiophenes over phosphorus modified CoMo/Al_2O_3 catalysts. *Fuel. Process. Technol.* **2012**, *98*, 39–44. [CrossRef]
144. Gao, Q.; Ofosu, T.N.; Ma, S.-G.; Komvokis, V.G.; Williams, C.T.; Segawa, K. Catalyst development for ultra-deep hydrodesulfurization (HDS) of dibenzothiophenes. I: Effects of Ni promotion in molybdenum-based catalysts. *Catal. Today* **2011**, *164*, 538–543. [CrossRef]
145. Fujikawa, T.; Kimura, H.; Kiriyama, K.; Hagiwara, K. Development of ultra-deep HDS catalyst for production of clean diesel fuels. *Catal. Today* **2006**, *111*, 188–193. [CrossRef]
146. Farag, H.; Mochida, I. A comparative kinetic study on ultra-deep hydrodesulfurization of pre-treated gas oil over nanosized MoS_2, CoMo-sulfide, and commercial CoMo/Al_2O_3 catalysts. *J. Colloid Interface Sci.* **2012**, *372*, 121–129. [CrossRef] [PubMed]

147. Zhang, Y.; Yang, Y.; Han, H.; Yang, M.; Wang, L.; Zhang, Y.; Jiang, Z.; Li, C. Ultra-deep desulfurization via reactive adsorption on Ni/ZnO: The effect of ZnO particle size on the adsorption performance. *Appl. Catal. B* **2012**, *119*, 13–19. [CrossRef]
148. Petzold, F.G.; Jasinski, J.; Clark, E.L.; Kim, J.H.; Absher, J.; Toufar, H.; Sunkara, M.K. Nickel supported on zinc oxide nanowires as advanced hydrodesulfurization catalysts. *Catal. Today* **2012**, *198*, 219–227. [CrossRef]
149. Tang, G.; Tian, S.; Zhou, Z.; Wen, Y.; Pang, A.; Zhang, Y.; Zeng, D.; Li, H.; Shan, B.; Xie, C. ZnO micro/nanocrystals with tunable exposed (0001) facets for enhanced catalytic activity on the thermal decomposition of ammonium perchlorate. *J. Phys. Chem. C* **2014**, *118*, 11833–11841. [CrossRef]
150. Hariharan, C. Photocatalytic degradation of organic contaminants in water by ZnO nanoparticles: Revisited. *Appl. Catal. A* **2006**, *304*, 55–61. [CrossRef]
151. Chong, M.N.; Jin, B.; Chow, C.W.K.; Saint, C. Recent developments in photocatalytic water treatment technology: A review. *Water. Res.* **2010**, *44*, 2997–3027. [CrossRef] [PubMed]
152. Wu, C.; Shen, L.; Yu, H.; Huang, Q.; Zhang, Y.C. Synthesis of Sn-doped ZnO nanorods and their photocatalytic properties. *Mater. Res. Bull.* **2011**, *46*, 1107–1112. [CrossRef]
153. Panthi, G.; Park, M.; Kim, H.-Y.; Lee, S.-Y.; Park, S.-J. Electrospun ZnO hybrid nanofibers for photodegradation of wastewater containing organic dyes: A review. *J. Ind. Eng. Chem.* **2015**, *21*, 26–35. [CrossRef]
154. Wang, Y.; Wang, Q.; Zhan, X.; Wang, F.; Safdar, M.; He, J. Visible light driven type II heterostructures and their enhanced photocatalysis properties: A review. *Nanoscale* **2013**, *5*, 8326–8339. [CrossRef] [PubMed]
155. Lam, S.-M.; Sin, J.-C.; Abdullah, A.Z.; Mohamed, A.R. Degradation of wastewaters containing organic dyes photocatalysed by zinc oxide: A review. *Desalin. Water Treat.* **2012**, *41*, 131–169. [CrossRef]
156. Souza, R.P.; Freitas, T.K.F.S.; Domingues, F.S.; Pezoti, O.; Ambrosio, E.; Ferrari-Lima, A.M.; Garcia, J.C. Photocatalytic activity of TiO_2, ZnO and Nb_2O_5 applied to degradation of textile wastewater. *J. Photochem. Photobiol. A* **2016**, *329*, 9–17. [CrossRef]
157. Elmolla, E.S.; Chaudhuri, M. Degradation of amoxicillin, ampicillin and cloxacillin antibiotics in aqueous solution by the UV/ZnO photocatalytic process. *J. Hazard. Mater.* **2010**, *173*, 445–449. [CrossRef] [PubMed]
158. Pardeshi, S.; Patil, A. Effect of morphology and crystallite size on solar photocatalytic activity of zinc oxide synthesized by solution free mechanochemical method. *J. Mol. Catal. A Chem.* **2009**, *308*, 32–40. [CrossRef]
159. Ali, A.M.; Emanuelsson, E.A.; Patterson, D.A. Photocatalysis with nanostructured zinc oxide thin films: The relationship between morphology and photocatalytic activity under oxygen limited and oxygen rich conditions and evidence for a mars van krevelen mechanism. *Appl. Catal. B* **2010**, *97*, 168–181. [CrossRef]
160. Ullah, R.; Dutta, J. Photocatalytic degradation of organic dyes with manganese-doped ZnO nanoparticles. *J. Hazard. Mater.* **2008**, *156*, 194–200. [CrossRef] [PubMed]
161. Lin, Y.-G.; Hsu, Y.-K.; Chen, Y.-C.; Chen, L.-C.; Chen, S.-Y.; Chen, K.-H. Visible-light-driven photocatalytic carbon-doped porous ZnO nanoarchitectures for solar water-splitting. *Nanoscale* **2012**, *4*, 6515–6519. [CrossRef] [PubMed]
162. Kumar, S.; Baruah, A.; Tonda, S.; Kumar, B.; Shanker, V.; Sreedhar, B. Cost-effective and eco-friendly synthesis of novel and stable N-doped ZnO/g-C_3N_4 core-shell nanoplates with excellent visible-light responsive photocatalysis. *Nanoscale* **2014**, *6*, 4830–4842. [CrossRef] [PubMed]
163. Kochuveedu, S.T.; Jang, Y.H.; Jang, Y.J.; Kim, D.H. Visible light active photocatalysis on block copolymer induced strings of ZnO nanoparticles doped with carbon. *J. Mater. Chem. A* **2013**, *1*, 898–905. [CrossRef]
164. Kadam, S.R.; Mate, V.R.; Panmand, R.P.; Nikam, L.K.; Kulkarni, M.V.; Sonawane, R.S.; Kale, B.B. A green process for efficient lignin (biomass) degradation and hydrogen production via water splitting using nanostructured C, N, S-doped ZnO under solar light. *RSC Adv.* **2014**, *4*, 60626–60635. [CrossRef]
165. Geng, B.Y.; Wang, G.Z.; Jiang, Z.; Xie, T.; Sun, S.H.; Meng, G.W.; Zhang, L.D. Synthesis and optical properties of S-doped zno nanowires. *Appl. Phys. Lett.* **2003**, *82*, 4791–4793. [CrossRef]
166. Cho, S.; Jang, J.-W.; Lee, J.S.; Lee, K.-H. Carbon-doped ZnO nanostructures synthesized using vitamin C for visible light photocatalysis. *CrystEngComm* **2010**, *12*, 3929–3935. [CrossRef]
167. Bhirud, A.P.; Sathaye, S.D.; Waichal, R.P.; Nikam, L.K.; Kale, B.B. An eco-friendly, highly stable and efficient nanostructured p-type N-doped ZnO photocatalyst for environmentally benign solar hydrogen production. *Green Chem.* **2012**, *14*, 2790–2798. [CrossRef]
168. Bae, S.Y.; Seo, H.W.; Park, J. Vertically aligned sulfur-doped ZnO nanowires synthesized via chemical vapor deposition. *J. Phys. Chem. B* **2004**, *108*, 5206–5210. [CrossRef]

169. Jang, Y.J.; Simer, C.; Ohm, T. Comparison of zinc oxide nanoparticles and its nano-crystalline particles on the photocatalytic degradation of methylene blue. *Mater. Res. Bull.* **2006**, *41*, 67–77. [CrossRef]
170. Zhang, L.; Yin, L.; Wang, C.; Lun, N.; Qi, Y. Sol-gel growth of hexagonal faceted ZnO prism quantum dots with polar surfaces for enhanced photocatalytic activity. *ACS Appl. Mater. Int.* **2010**, *2*, 1769–1773. [CrossRef] [PubMed]
171. Mclaren, A.; Valdes-Solis, T.; Li, G.; Tsang, S.C. Shape and size effects of ZnO nanocrystals on photocatalytic activity. *J. Am. Chem. Soc.* **2009**, *131*, 12540–12541. [CrossRef] [PubMed]
172. Duan, J.; Liu, X.; Han, Q.; Wang, X. Controlled morphologies and optical properties of ZnO films and their photocatalytic activities. *J. Alloys Compd.* **2011**, *509*, 9255–9263. [CrossRef]
173. Boppella, R.; Anjaneyulu, K.; Basak, P.; Manorama, S.V. Facile synthesis of face oriented ZnO crystals: Tunable polar facets and shape induced enhanced photocatalytic performance. *J. Phys. Chem. C* **2013**, *117*, 4597–4605. [CrossRef]
174. Pudukudy, M.; Yaakob, Z. Facile solid state synthesis of zno hexagonal nanogranules with excellent photocatalytic activity. *Appl. Surface Sci.* **2014**, *292*, 520–530. [CrossRef]
175. Lv, Y.; Yao, W.; Ma, X.; Pan, C.; Zong, R.; Zhu, Y. The surface oxygen vacancy induced visible activity and enhanced UV activity of a ZnO_{1-x} photocatalyst. *Catal. Sci. Technol.* **2013**, *3*, 3136–3146. [CrossRef]
176. Shidpour, R.; Simchi, A.; Ghanbari, F.; Vossoughi, M. Photo-degradation of organic dye by zinc oxide nanosystems with special defect structure: Effect of the morphology and annealing temperature. *Appl. Catal. A* **2014**, *472*, 198–204. [CrossRef]
177. Liu, T.-J.; Wang, Q.; Jiang, P. Morphology-dependent photo-catalysis of bare zinc oxide nanocrystals. *RSC Adv.* **2013**, *3*, 12662–12670. [CrossRef]
178. Ranjith, K.S.; Rajendra Kumar, R.T. Surfactant free, simple, morphological and defect engineered ZnO nanocatalyst: Effective study on sunlight driven and reusable photocatalytic properties. *J. Photochem. Photobiol. B* **2016**, *329*, 35–45. [CrossRef]
179. Jeong, H.W.; Choi, S.-Y.; Hong, S.H.; Lim, S.K.; Han, D.S.; Abdel-Wahab, A.; Park, H. Shape-dependent charge transfers in crystalline ZnO photocatalysts: Rods versus plates. *J. Phys. Chem. C* **2014**, *118*, 21331–21338. [CrossRef]
180. Khokhra, R.; Singh, R.K.; Kumar, R. Effect of synthesis medium on aggregation tendencies of ZnO nanosheets and their superior photocatalytic performance. *J. Mater. Sci.* **2015**, *50*, 819–832. [CrossRef]
181. Wang, X.; Zhang, Q.; Wan, Q.; Dai, G.; Zhou, C.; Zou, B. Controllable ZnO architectures by ethanol amine-assisted hydrothermal reaction for enhanced photocatalytic activity. *J. Phys. Chem. C* **2011**, *115*, 2769–2775. [CrossRef]
182. Kuriakose, S.; Satpati, B.; Mohapatra, S. Enhanced photocatalytic activity of Co doped ZnO nanodisks and nanorods prepared by a facile wet chemical method. *Phys. Chem. Chem. Phys.* **2014**, *16*, 12741–12749. [CrossRef] [PubMed]
183. Rajbongshi, B.M.; Samdarshi, S.K. ZnO and CO-ZnO nanorods—Complementary role of oxygen vacancy in photocatalytic activity of under UV and visible radiation flux. *Mater. Sci. Eng. B* **2014**, *182*, 21–28. [CrossRef]
184. Pawar, R.C.; Choi, D.-H.; Lee, J.-S.; Lee, C.S. Formation of polar surfaces in microstructured ZnO by doping with Cu and applications in photocatalysis using visible light. *Mater. Chem. Phys.* **2015**, *151*, 167–180. [CrossRef]
185. Han, Z.; Li, S.; Chu, J.; Chen, Y. Electrospun pd-doped ZnO nanofibers for enhanced photocatalytic degradation of methylene blue. *J. Sol-Gel Sci. Technol.* **2013**, *66*, 139–144. [CrossRef]
186. Faisal, M.; Ismail, A.A.; Ibrahim, A.A.; Bouzid, H.; Al-Sayari, S.A. Highly efficient photocatalyst based on Ce doped ZnO nanorods: Controllable synthesis and enhanced photocatalytic activity. *Chem. Eng. J.* **2013**, *229*, 225–233. [CrossRef]
187. Sun, L.; Zhao, D.; Song, Z.; Shan, C.; Zhang, Z.; Li, B.; Shen, D. Gold nanoparticles modified ZnO nanorods with improved photocatalytic activity. *J. Colloid. Interface Sci.* **2011**, *363*, 175–181. [CrossRef]
188. Egelhaaf, H.-J.; Oelkrug, D. Luminescence and nonradiative deactivation of excited states involving oxygen defect centers in polycrystalline ZnO. *J. Cryst. Growth* **1996**, *161*, 190–194. [CrossRef]
189. Goto, H.; Hanada, Y.; Ohno, T.; Matsumura, M. Quantitative analysis of superoxide Ion and hydrogen peroxide produced from molecular oxygen on photoirradiated TiO_2 particles. *J. Catal.* **2004**, *225*, 223–229. [CrossRef]

190. Subramanian, V.; Wolf, E.E.; Kamat, P.V. Green emission to probe photoinduced charging events in ZnO-Au nanoparticles. Charge distribution and fermi-level equilibration. *J. Phys. Chem. B* **2003**, *107*, 7479–7485. [CrossRef]
191. Kayaci, F.; Vempati, S.; Ozgit-Akgun, C.; Biyikli, N.; Uyar, T. Enhanced photocatalytic activity of homoassembled ZnO nanostructures on electrospun polymeric nanofibers: A combination of atomic layer deposition and hydrothermal growth. *Appl. Catal. B* **2014**, *156*, 173–183. [CrossRef]
192. Zhu, G.; Wang, H.; Yang, G.; Chen, L.; Guo, P.; Zhang, L. A facile synthesis of ZnO/CNT hierarchical microsphere composites with enhanced photocatalytic degradation of methylene blue. *RSC Adv.* **2015**, *5*, 72476–72481. [CrossRef]
193. Chang, Y.-C. Complex ZnO/ZnS nanocable and nanotube arrays with high performance photocatalytic activity. *J. Alloys Compd.* **2016**, *664*, 538–546. [CrossRef]
194. Avci, A.; Eskizeybek, V.; Gülce, H.; Haspulat, B.; Şahin, Ö.S. ZnO-TiO_2 nanocomposites formed under submerged dc arc discharge: Preparation, characterization and photocatalytic properties. *Appl. Phys. A* **2014**, *116*, 1119–1125. [CrossRef]
195. Wang, M.H.; Cui, L.Y.; Li, S.Y.; Li, Z.X.; Ma, T.L.; Luan, G.Y.; Liu, W.; Zhang, F.L. Facile fabrication hybrids of TiO_2@ZnO tubes with enhanced photocatalytic properties. *RSC Adv.* **2016**, *6*, 58452–58457. [CrossRef]
196. Liu, X.; Huang, W.; Cheng, H.; Huang, B.; Bai, D.; Fu, F.; Wu, H.; Li, L. In-situ observation of hydrothermal growth of ZnO nanowires on patterned Zn substrate and their photocatalytic performance. *Appl. Surface Sci.* **2015**, *356*, 240–248. [CrossRef]
197. Lu, J.; Wang, H.; Peng, D.; Chen, T.; Dong, S.; Chang, Y. Synthesis and properties of Au/ZnO nanorods as a plasmonic photocatalyst. *Phys. E* **2016**, *78*, 41–48. [CrossRef]
198. Li, C.; Ahmed, T.; Ma, M.; Edvinsson, T.; Zhu, J. A facile approach to ZnO/CdS nanoarrays and their photocatalytic and photoelectrochemical properties. *Appl. Catal. B* **2013**, *138*, 175–183. [CrossRef]
199. Li, G.; Yi, Z.; Wang, H.; Jia, C.; Zhang, W. Factors impacted on anisotropic photocatalytic oxidization activity of ZnO: Surface band bending, surface free energy and surface conductance. *Appl. Catal. B* **2014**, *158–159*, 280–285. [CrossRef]
200. Yang, J.; Wang, J.; Li, X.; Lang, J.; Liu, F.; Yang, L.; Zhai, H.; Gao, M.; Zhao, X. Effect of polar and non-polar surfaces of ZnO nanostructures on photocatalytic properties. *J. Alloys Compd.* **2012**, *528*, 28–33. [CrossRef]
201. Li, X.; Wang, J.; Yang, J.; Lang, J.; Lü, S.; Wei, M.; Meng, X.; Kou, C.; Li, X. Comparison of photocatalytic activity of ZnO rod arrays with various diameter sizes and orientation. *J. Alloys Compd.* **2013**, *580*, 205–210. [CrossRef]
202. Li, X.; Wang, J.; Yang, J.; Lang, J.; Cao, J.; Liu, F.; Fan, H.; Gao, M.; Jiang, Y. Size-controlled fabrication of ZnO micro/nanorod arrays and their photocatalytic performance. *Mater. Chem. Phys.* **2013**, *141*, 929–935. [CrossRef]
203. Subash, B.; Krishnakumar, B.; Swaminathan, M.; Shanthi, M. Enhanced photocatalytic performance of WO_3 loaded Ag–ZnO for acid black 1 degradation by UV-a light. *J. Mol. Catal. A Chem.* **2013**, *366*, 54–63. [CrossRef]
204. Li, D.; Haneda, H. Enhancement of photocatalytic activity of sprayed nitrogen-containing ZnO powders by coupling with metal oxides during the acetaldehyde decomposition. *Chemosphere* **2004**, *54*, 1099–1110. [CrossRef] [PubMed]
205. Danwittayakul, S.; Jaisai, M.; Koottatep, T.; Dutta, J. Enhancement of photocatalytic degradation of methyl orange by supported zinc oxide nanorods/zinc stannate (ZnO/ZTO) on porous substrates. *Ind. Eng. Chem. Res.* **2013**, *52*, 13629–13636. [CrossRef]
206. Gong, W.; Pan, G.; Shang, F.; Wang, F.; Zhou, Z.; Liu, C.; Zhao, M.; Zi, Z.; Wei, Y.; Lv, J.; et al. Effect of ethylene glycol monomethyl ether ratio in mixed solvent on surface morphology, wet ability and photocatalytic properties of ZnO thin films. *J. Mater. Sci.-Mater. El.* **2014**, *25*, 2948–2956. [CrossRef]
207. Chen, Y.; Zhang, L.; Ning, L.; Zhang, C.; Zhao, H.; Liu, B.; Yang, H. Superior photocatalytic activity of porous wurtzite ZnO nanosheets with exposed {001} facets and a charge separation model between polar (001) and $(00\bar{1})$ surfaces. *Chem. Eng. J.* **2015**, *264*, 557–564. [CrossRef]
208. Hong, Y.; Tian, C.; Jiang, B.; Wu, A.; Zhang, Q.; Tian, G.; Fu, H. Facile synthesis of sheet-like ZnO assembly composed of small ZnO particles for highly efficient photocatalysis. *J. Mater. Chem.* **2013**, *1*, 5700–5708. [CrossRef]

209. Xiao, S.; Li, H.; Liu, L.; Lian, J. Glucose-assisted generation of assembled mesoporous ZnO sheets with highly efficient photocatalytic performance. *Mater. Sci. Semicond. Process.* **2015**, *39*, 680–685. [CrossRef]
210. Chen, Y.-C.; Lo, S.-L. Effects of operational conditions of microwave-assisted synthesis on morphology and photocatalytic capability of zinc oxide. *Chem. Eng. J.* **2011**, *170*, 411–418. [CrossRef]
211. Gomez-Solís, C.; Ballesteros, J.; Torres-Martínez, L.; Juárez-Ramírez, I.; Torres, L.D.; Zarazua-Morin, M.E.; Lee, S.W. Rapid synthesis of ZnO nano-corncobs from nital solution and its application in the photodegradation of methyl orange. *J. Photochem. Photobiol. B* **2015**, *298*, 49–54. [CrossRef]
212. Srikhaow, A.; Smith, S.M. Photocatalytic activity of flower-like ZnO derived by a d-glucose-assisted sonochemical method. *Res. Chem. Intermed.* **2013**, *39*, 1545–1553. [CrossRef]
213. Misra, M.; Kapur, P.; Singla, M.L. Surface plasmon quenched of near band edge emission and enhanced visible photocatalytic activity of Au@ZnO core-shell nanostructure. *Appl. Catal. B* **2014**, *150*, 605–611. [CrossRef]
214. Xiao, S.; Zhao, L.; Lian, J. Enhanced photocatalytic performance of supported Fe doped ZnO nanorod arrays prepared by wet chemical method. *Catal. Lett.* **2014**, *144*, 347–354. [CrossRef]
215. Huang, J.; Liu, S.; Kuang, L.; Zhao, Y.; Jiang, T.; Liu, S.; Xu, X. Enhanced photocatalytic activity of quantum-dot-sensitized one-dimensionally-ordered ZnO nanorod photocatalyst. *J. Environ. Sci.* **2013**, *25*, 2487–2491. [CrossRef]
216. Lu, F.; Cai, W.; Zhang, Y. Zno hierarchical micro/nanoarchitectures: Solvothermal synthesis and structurally enhanced photocatalytic performance. *Adv. Funct. Mater.* **2008**, *18*, 1047–1056. [CrossRef]
217. Lu, H.; Wang, S.; Zhao, L.; Li, J.; Dong, B.; Xu, Z. Hierarchical ZnO microarchitectures assembled by ultrathin nanosheets: Hydrothermal synthesis and enhanced photocatalytic activity. *J. Mater. Chem.* **2011**, *21*, 4228–4234. [CrossRef]
218. Lin, L.; Yang, Y.C.; Men, L.; Wang, X.; He, D.N.; Chai, Y.C.; Zhao, B.; Ghoshroy, S.; Tang, Q.W. A highly efficient TiO_2@ZnO n-p-n heterojunction nanorod photocatalyst. *Nanoscale* **2013**, *5*, 588–593. [CrossRef] [PubMed]
219. Yi, S.; Zhao, F.; Yue, X.; Wang, D.; Lin, Y. Enhanced solar light-driven photocatalytic activity of BiOBr–ZnO heterojunctions with effective separation and transfer properties of photo-generated chargers. *New J. Chem.* **2015**, *39*, 6659–6666. [CrossRef]
220. Huang, M.; Yan, Y.; Feng, W.; Weng, S.; Zheng, Z.; Fu, X.; Liu, P. Controllable tuning various ratios of ZnO polar facets by crystal seed-assisted growth and their photocatalytic activity. *Cryst. Growth Des.* **2014**, *14*, 2179–2186. [CrossRef]
221. Wang, J.; Xia, Y.; Dong, Y.; Chen, R.; Xiang, L.; Komarneni, S. Defect-rich ZnO nanosheets of high surface area as an efficient visible-light photocatalyst. *Appl. Catal. B* **2016**, *192*, 8–16. [CrossRef]
222. Fan, J.; Li, T.; Heng, H. Hydrothermal growth of ZnO nanoflowers and their photocatalyst application. *Bull. Mater. Sci.* **2016**, *39*, 19–26. [CrossRef]
223. Li, X.; Wang, J.; Yang, J.; Lang, J.; Wei, M.; Meng, X.; Lü, S.; Sui, Y. Enhanced photocatalytic activity of ZnO microflower arrays synthesized by one-step etching approach. *J. Mol. Catal. A Chem.* **2013**, *378*, 1–6. [CrossRef]
224. Lu, Y.; Wang, L.; Wang, D.; Xie, T.; Chen, L.; Lin, Y. A comparative study on plate-like and flower-like ZnO nanocrystals surface photovoltage property and photocatalytic activity. *Mater. Chem. Phys.* **2011**, *129*, 281–287. [CrossRef]
225. Li, B.X.; Wang, Y.F. Facile Synthesis and Enhanced Photocatalytic Performance of Flower-like ZnO Hierarchical Microstructures. *J. Phys. Chem. C* **2010**, *114*, 890–896. [CrossRef]
226. Guo, Y.; Lin, S.; Li, X.; Liu, Y. Amino acids assisted hydrothermal synthesis of hierarchically structured ZnO with enhanced photocatalytic activities. *Appl. Surface Sci.* **2016**, *384*, 83–91. [CrossRef]
227. Wang, S.W.; Yu, Y.; Zuo, Y.H.; Li, C.Z.; Yang, J.H.; Lu, C.H. Synthesis and photocatalysis of hierarchical heteroassemblies of ZnO branched nanorod arrays on Ag core nanowires. *Nanoscale* **2012**, *4*, 5895–5901. [CrossRef] [PubMed]
228. Liang, Y.; Guo, N.; Li, L.; Li, R.; Ji, G.; Gan, S. Fabrication of porous 3D flower-like Ag/ZnO heterostructure composites with enhanced photocatalytic performance. *Appl. Surface Sci.* **2015**, *332*, 32–39. [CrossRef]
229. Wu, Z.; Wang, H.; Xue, Y.; Li, B.; Geng, B. ZnO nanorods/ZnSe heteronanostructure arrays with a tunable microstructure of ZnSe shell for visible light photocatalysis. *J. Mater. Chem.* **2014**, *2*, 17502–17510. [CrossRef]

230. Chennakesavulu, K.; Reddy, M.M.; Reddy, G.R.; Rabel, A.; Brijitta, J.; Vinita, V.; Sasipraba, T.; Sreeramulu, J. Synthesis, characterization and photo catalytic studies of the composites by tantalum oxide and zinc oxide nanorods. *J. Mol. Struct.* **2015**, *1091*, 49–56. [CrossRef]
231. Li, X.; Hu, Z.; Liu, J.; Li, D.; Zhang, X.; Chen, J.; Fang, J. Ga doped ZnO photonic crystals with enhanced photocatalytic activity and its reaction mechanism. *Appl. Catal. B* **2016**, *195*, 29–38. [CrossRef]
232. Yin, Q.; Qiao, R.; Li, Z.; Zhang, X.L.; Zhu, L. Hierarchical nanostructures of nickel-doped zinc oxide: Morphology controlled synthesis and enhanced visible-light photocatalytic activity. *J. Alloys Compd.* **2015**, *618*, 318–325. [CrossRef]
233. Yin, Q.; Wu, W.; Qiao, R.; Ke, X.; Hu, Y.; Li, Z. Glucose-assisted transformation of Ni-doped-ZnO@carbon to a Ni-doped-ZnO@void@SiO_2 core–shell nanocomposite photocatalyst. *RSC Adv.* **2016**, *6*, 38653–38661. [CrossRef]
234. Liang, Y.; Guo, N.; Li, L.; Li, R.; Ji, G.; Gan, S. Preparation of porous 3D Ce-doped ZnO microflowers with enhanced photocatalytic performance. *RSC Adv.* **2015**, *5*, 59887–59894. [CrossRef]
235. Chandrasekhar, M.; Nagabhushana, H.; Vidya, Y.; Anantharaju, K.; Sharma, S.; Premkumar, H.; Prashantha, S.; Prasad, B.D.; Shivakumara, C.; Saraf, R. Synthesis of Eu^{3+}-activated ZnO superstructures: Photoluminescence, judd-ofelt analysis and sunlight photocatalytic properties. *J. Mol. Catal. A Chem.* **2015**, *409*, 26–41. [CrossRef]
236. Wang, Y.; Cheng, J.; Yu, S.; Alcocer, E.J.; Shahid, M.; Wang, Z.; Pan, W. Synergistic effect of N-decorated and Mn^{2+} doped ZnO nanofibers with enhanced photocatalytic activity. *Sci. Rep.* **2016**, *6*, 32711. [CrossRef] [PubMed]
237. Cho, S.; Kim, S.; Jang, J.-W.; Jung, S.-H.; Oh, E.; Lee, B.R.; Lee, K.-H. Large-scale fabrication of sub-20-nm-diameter ZnO nanorod arrays at room temperature and their photocatalytic activity. *J. Phys. Chem. C* **2009**, *113*, 10452–10458. [CrossRef]
238. Hafez, H.S. Highly active ZnO rod-like nanomaterials: Synthesis, characterization and photocatalytic activity for dye removal. *Phys. E* **2012**, *44*, 1522–1527. [CrossRef]
239. Leelavathi, A.; Madras, G.; Ravishankar, N. Origin of enhanced photocatalytic activity and photoconduction in high aspect ratio ZnO nanorods. *Phys. Chem. Chem. Phys.* **2013**, *15*, 10795–10802. [CrossRef] [PubMed]
240. Srinivasan, P.; Subramanian, B.; Djaoued, Y.; Robichaud, J.; Sharma, T.; Bruning, R. Facile synthesis of mesoporous nanocrystalline ZnO bipyramids and spheres: Characterization, and photocatalytic activity. *Mater. Chem. Phys.* **2015**, *155*, 162–170. [CrossRef]
241. Lan, S.; Liu, L.; Li, R.; Leng, Z.; Gan, S. Hierarchical hollow structure ZnO: Synthesis, characterization, and highly efficient adsorption/photocatalysis toward congo red. *Ind. Eng. Chem. Res.* **2014**, *53*, 3131–3139. [CrossRef]
242. Mousavi, S.M.; Mahjoub, A.R.; Abazari, R. Green synthesis of ZnO hollow sphere nanostructures by a facile route at room temperature with efficient photocatalytic dye degradation properties. *RSC Adv.* **2015**, *5*, 107378–107388. [CrossRef]
243. Yu, C.; Yang, K.; Xie, Y.; Fan, Q.; Jimmy, C.Y.; Shu, Q.; Wang, C. Novel hollow Pt-ZnO nanocomposite microspheres with hierarchical structure and enhanced photocatalytic activity and stability. *Nanoscale* **2013**, *5*, 2142–2151. [CrossRef] [PubMed]
244. Lamba, R.; Umar, A.; Mehta, S.K.; Anderson, W.A.; Kansal, S.K. Visible-light-driven photocatalytic properties of self assembled cauliflower-like AgCl/ZnO hierarchical nanostructures. *J. Mol. Catal. A Chem.* **2015**, *408*, 189–201. [CrossRef]
245. Lamba, R.; Umar, A.; Mehta, S.K.; Kansal, S.K. CeO_2-ZnO hexagonal nanodisks: Efficient material for the degradation of direct blue 15 dye and its simulated dye bath effluent under solar light. *J. Alloys. Compd.* **2015**, *620*, 67–73. [CrossRef]
246. Mohan, R.; Krishnamoorthy, K.; Kim, S.-J. Enhanced photocatalytic activity of Cu-doped ZnO nanorods. *Solid State Commun.* **2012**, *152*, 375–380. [CrossRef]
247. Wan, X.; Liang, X.; Zhang, C.; Li, X.; Liang, W.; Xu, H.; Lan, S.; Tie, S. Morphology controlled syntheses of Cu-doped ZnO, tubular Zn(Cu)O and Ag decorated tubular Zn(Cu)O microcrystals for photocatalysis. *Chem. Eng. J.* **2015**, *272*, 58–68. [CrossRef]
248. Xu, F.; Yuan, Z.-Y.; Du, G.-H.; Halasa, M.; Su, B.-L. High-yield synthesis of single-crystalline ZnO hexagonal nanoplates and accounts of their optical and photocatalytic properties. *Appl. Phys. A* **2007**, *86*, 181–185. [CrossRef]

249. Liu, D.; Lv, Y.; Zhang, M.; Liu, Y.; Zhu, Y.; Zong, R.; Zhu, Y. Defect-related photoluminescence and photocatalytic properties of porous ZnO nanosheets. *J. Mater. Chem.* **2014**, *2*, 15377–15388. [CrossRef]
250. Clament Sagaya Selvam, N.; Vijaya, J.J.; Kennedy, L.J. Effects of morphology and Zr doping on structural, optical, and photocatalytic properties of ZnO nanostructures. *Ind. Eng. Chem. Res.* **2012**, *51*, 16333–16345. [CrossRef]
251. Rezapour, M.; Talebian, N. Comparison of structural, optical properties and photocatalytic activity of ZnO with different morphologies: Effect of synthesis methods and reaction media. *Mater. Chem. Phys.* **2011**, *129*, 249–255. [CrossRef]
252. Lam, S.-M.; Sin, J.-C.; Satoshi, I.; Abdullah, A.Z.; Mohamed, A.R. Enhanced sunlight photocatalytic performance over Nb_2O_5/ZnO nanorod composites and the mechanism study. *Appl. Catal. A* **2014**, *471*, 126–135. [CrossRef]
253. Lam, S.-M.; Sin, J.-C.; Mohamed, A.R. Fabrication of ZnO nanorods via a green hydrothermal method and their light driven catalytic activity towards the erasure of phenol compounds. *Mater. Lett.* **2016**, *167*, 141–144. [CrossRef]
254. Wu, S.-Z.; Li, N.; Zhang, W.-D. Attachment of ZnO nanoparticles onto layered double hydroxides microspheres for high performance photocatalysis. *J. Porous Mater.* **2014**, *21*, 157–164. [CrossRef]
255. Sin, J.-C.; Lam, S.-M.; Lee, K.-T.; Mohamed, A.R. Preparation and photocatalytic properties of visible light-driven samarium-doped ZnO nanorods. *Ceram. Int.* **2013**, *39*, 5833–5843. [CrossRef]
256. Sin, J.-C.; Lam, S.-M.; Lee, K.-T.; Mohamed, A.R. Preparation of rare earth-doped ZnO hierarchical micro/nanospheres and their enhanced photocatalytic activity under visible light irradiation. *Ceram. Int.* **2014**, *40*, 5431–5440. [CrossRef]
257. Sin, J.-C.; Lam, S.-M.; Satoshi, I.; Lee, K.-T.; Mohamed, A.R. Sunlight photocatalytic activity enhancement and mechanism of novel europium-doped ZnO hierarchical micro/nanospheres for degradation of phenol. *Appl. Catal. B* **2014**, *148*, 258–268. [CrossRef]
258. Sin, J.-C.; Lam, S.-M.; Lee, K.-T.; Mohamed, A.R. Preparation of cerium-doped ZnO hierarchical micro/nanospheres with enhanced photocatalytic performance for phenol degradation under visible light. *J. Mol. Catal. A Chem.* **2015**, *409*, 1–10. [CrossRef]
259. Sin, J.-C.; Lam, S.-M.; Lee, K.-T.; Mohamed, A.R. Photocatalytic performance of novel samarium-doped spherical-like ZnO hierarchical nanostructures under visible light irradiation for 2,4-dichlorophenol degradation. *J. Colloid Interface Sci.* **2013**, *401*, 40–49. [CrossRef] [PubMed]
260. Ba-Abbad, M.M.; Kadhum, A.A.H.; Mohamad, A.B.; Takriff, M.S.; Sopian, K. Visible light photocatalytic activity of Fe^{3+}-doped ZnO nanoparticle prepared via Sol-Gel technique. *Chemosphere* **2013**, *91*, 1604–1611. [CrossRef] [PubMed]
261. Tang, Z.-R.; Yin, X.; Zhang, Y.; Xu, Y.-J. One-pot, high-yield synthesis of one-dimensional ZnO nanorods with well-defined morphology as a highly selective photocatalyst. *RSC Adv.* **2013**, *3*, 5956–5965. [CrossRef]
262. Pan, X.; Yang, M.-Q.; Xu, Y.-J. Morphology control, defect engineering and photoactivity tuning of ZnO crystals by graphene oxide–a unique 2D macromolecular surfactant. *Phys. Chem. Chem. Phys.* **2014**, *16*, 5589–5599. [CrossRef] [PubMed]
263. Yu, W.; Zhang, J.; Peng, T. New insight into the enhanced photocatalytic activity of N-, C- and S-doped ZnO photocatalysts. *Appl. Catal. B* **2016**, *181*, 220–227. [CrossRef]
264. Liao, F.; Zeng, Z.; Eley, C.; Lu, Q.; Hong, X.; Tsang, S.C. Electronic modulation of a copper/zinc oxide catalyst by a heterojunction for selective hydrogenation of carbon dioxide to methanol. *Angew. Chem. Int. Ed.* **2012**, *51*, 5832–5836. [CrossRef] [PubMed]